Non-invasive cardiac radiosurgery with MRI guidance:

A ground-truth for real-time target localisation using the XCAT phantom

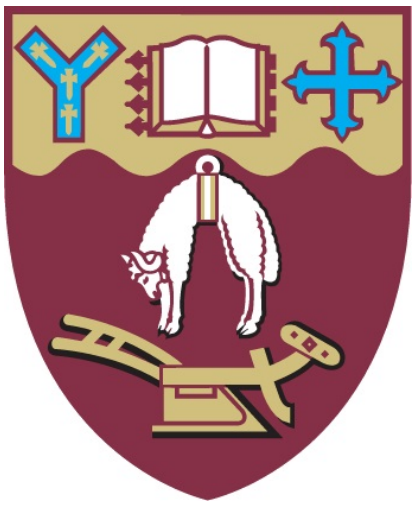

Nicholas John Lowther

Department of Physics and Astronomy
University of Canterbury

This dissertation is submitted for the degree of
Master of Science in Medical Physics

April 2016

DECLARATION

I hereby declare that except where specific reference is made to the work of others, the contents of this dissertation are original and have not been submitted in whole or in part for consideration for any other degree or qualification in this, or any other university.

Nicholas John Lowther
April 2016

ACKNOWLEDGEMENTS

This thesis is the result of the first collaboration between the University of Canterbury, New Zealand and the Radiation Physics Laboratory at the University of Sydney, Australia. I am extremely fortunate and thankful for the opportunity to work with this top class research group.

I like to thank and express admiration towards my supervisors Ms. Svenja Ipsen, Prof. Paul Keall and Dr. Steven Marsh. Firstly, Ms. Svenja Ipsen who first laid the foundations for the MRI cardiac tracking work through her ground-breaking research. Her technical insight and knowledge of the project has been invaluable. Secondly, Prof. Paul Keall who possesses a wealth of experience and understanding of medical physics research and always pointed me in the right direction. Lastly, Dr. Steven Marsh who first introduced me to the project and always provided perceptive discussion of the project.

Additionally, I would also like to thank Assoc Prof. Paul Segars from Duke University for providing the XCAT phantom software and Ms. Robba Rai of Liverpool Hospital for bouncing around MRI scan protocol ideas with me and conducting volunteer scans.

This research would not have been possible without the generous scholarship provided by the Todd Foundation that assists postgraduate research. I express my gratitude toward the family and foundation. Furthermore, the support from the University of Canterbury through their master's scholarship has been greatly appreciated.

ACADEMIC CONTRIBUTIONS

Over the course of this thesis work I have contributed to the Australian MRI-Linac project by establishing the first collaboration between the University of Canterbury and the Radiation Physics Laboratory at the University of Sydney. I hope this first collaboration can open the door for succeeding University of Canterbury students to become involved with the Radiation Physics Laboratory and its pioneering medical physics projects. I have also made the following contributions:

- Oral presentation of "A ground truth for volumetric MRI cardiac tracking using the XCAT phantom" at the *2015 Engineering & Physical Sciences in Medicine Conference (EPSM)*, 11th November 2015. This is the premier annual event for medical physicists and biomedical engineers in Australia and New Zealand held annually.
- Journal article. Ipsen, S. Lowther, N. Liney, G. Rades, D. Dunst, J. Schweikard, A. Keall, P. Blanck, O. MRI localization for cardiac radiosurgery: MRI real-time target localization for non-invasive cardiac radiosurgery in an integrated MRI linear accelerator. To be submitted to *Physics in Medicine and Biology*.
- Oral presentation of "A real-time cardiac MRI tracking technique based on template matching for the development of atrial fibrillation treatment with radiosurgery" at the *Medical Physics and Bioengineering (MPBE) fortnightly seminars at Christchurch Hospital*, 6th June 2015. Fortnightly seminar sessions allowing research to be shared with hospital staff and interested parties.
- Contributed to the oral presentation of "Echtzeit-Lokalisation in simulierten und realen MRT-Daten für nicht invasive Radiochirurgie des Herzens in einem MR-Linac". To be presented by Ms. Svenja Ipsen at the *47th annual meeting of the German Society of Medical Physics (DGMP)*, 7 - 10 September 2016, Wurzburg, Germany. Presentation regarding the current state of the overall project including results from this thesis.

ABSTRACT

Atrial fibrillation (AF) is the most prevalent cardiac arrhythmia. The growing epidemic of AF already affects millions of patients around the world and millions more are forecast to develop the condition in coming decades. The standard non-pharmacological treatment for AF is catheter ablation, an invasive and time consuming procedure. Non-invasive treatment of AF with radiosurgery has recently been put forward but is challenged by complex cardiac and respiratory motion. Compensating for target motion and treating in real-time could be realised with a MRI linear accelerator (MRI-Linac). A recent study developed methodology to track cardiac targets for this purpose but until now no measure of its accuracy has been accessible. In this investigation, the existing real-time cardiac tracking is quantified and developed on a digital phantom platform. It is first tested within a perfect digital scenario and then extended to a realistic anthropomorphic simulation. In a final experiment, developed tracking methods are applied to real-world anatomical data.

A total number of twenty-one virtual patients were generated with the 4 dimensional extended cardiac-torso (XCAT) phantom software and received magnetic resonance imaging (MRI) simulated cardiac scans. A 3D volume representing a distinct cardiac phase is comprised of 2D slices which cover the entire target area. These template volumes are matched through pixel similarity to 2D orthogonal real-time MRI planes to localise the target volume in real-time. One virtual patient represented ideal and thus unrealistic MRI scans to initially test the cardiac tracking. Twenty virtual patients were subjected to MRI scans that closely model the proposed real-world scenario. An available ground-truth is compared to target motion trajectories output from the cardiac tracking algorithm for the twenty-one virtual patients. The cardiac tracking methodology is simultaneously developed as a result of the quantitative measures. Additionally, the correlation and significance of the virtual patients' physiological parameters with tracking accuracy is investigated. Finally, the best performing tracking function is qualitatively assessed on a single patient's real-world MRI scans.

Employing a tracking method with the same basic methodology as the original tracking on

the twenty virtual patient cohort resulted in a mean 3D tracking error of 3.2 ± 1.7 mm. The three anatomical plane constituent errors were 1.3 ± 0.9 mm in the superior inferior (SI) plane, 1.4 ± 0.9 mm in the anterior posterior (AP) plane and 2.2 ± 1.8 mm in the left right (LR) plane. This result is in strong agreement with the inferred error of 3 - 4 mm from the previous study that was based on 2D quantification. After tracking developments were implemented, the best performing mean 3D tracking error of 2.9 ± 1.6 mm was ascertained. A patient's heart rate is the only anatomical parameter to show a significant linear relationship with tracking error (r=0.65, p-value = 0.0018). Comparing best performing tracking functions across the virtual patients show that the optimal tracking function is patient-specific. When the developed methods were reintroduced to a patient's MRI data the tracking accuracy was qualitatively assessed to have improved.

The results of the previous single patient treatment planning indicate that high-dose cardiac radiosurgery can be administered for the treatment of AF when safety margins are below 5 mm. The quantitative measures presented here demonstrate that real-time target localisation and motion compensation could successfully be implemented with an MRI-Linac. The conclusions of this work strongly encourage further development of the proposed AF treatment with non-invasive radiosurgery.

TABLE OF CONTENTS

LIST OF FIGURES

LIST OF TABLES

NOMENCLATURE

Acronyms / Abbreviations

2D *Two dimensional*

3D *Three dimensional*

4D *Four dimensional*

AF *Atrial fibrillation*

AP *Anterior posterior*

bpm *beats per minute*

CT *Computed tomography*

DAP *Dual all positions*

DAPDB *Dual all positions dynamic bordered*

DAPD *Dual all positions bordered*

DB *Dynamic bordered*

DICOM *Digital imaging and communications in medicine*

DLPB *Dual last position bordered*

DLPDB *Dual last position dynamic bordered*

DLP *Dual last position*

ECG *Electrocardiogram*

FDA *Food and Drug Administration*

FE *Finite-element*

FOV *Field-of-view*

LA *Left atrium*

linac *Linear accelerator*

LR *Left right*

MLC *Multi-leaf collimator*

MRI-Linac *MRI linear accelerator*

MRI *Magnetic resonance imaging*

MSCT *Multislice computed tomography*

NURBS *Non-uniform rational basis spline*

OAR *Organ at risk*

PTV *Planning target volume*

PV *Pulmonary veins*

RF *Radiofrequency*

RMS *Root-mean-square*

RTOG 0915 *Radiation Therapy Oncology Group, Protocol 0915*

SABR *Stereotactic ablative radiosurgery*

SI *Superior inferior*

SNR *Signal-to-noise ratio*

SSFP *Steady-state free precession*

STAR *Stereotactic arrhythmia radioablation*

SVM *Support vector machine*

TAP *Tri-all positions*

TE *Echo time*

TLP *Tri-last position*

TR *Repetition time*

TrueFISP *True fast imaging with steady state precession*

VT *Ventricular tachycardia*

XCAT *4 dimensional extended cardiac-torso*

1

INTRODUCTION

Atrial fibrillation (AF), the most abundant cardiac arrhythmia is epidemically contributing to higher rates of mortality, morbidity and quality of life impairment. Presence of AF is a strong risk factor of stroke, increasing significantly with age. Over 10% of global deaths are due to stroke alone and as a result, treatments for underlying conditions such as AF should constantly be developed and optimised. Uncoordinated electrical activity in the atria caused by re-entrant electrical signals from the pulmonary veins (PV) give rise to irregular atrial contraction. Electrical isolation of the PV from the left atrium (LA) is an effective treatment for AF. This is traditionally achieved with catheter induced lesions of PV musculature. However, the procedure is time-consuming, complex and invasive. Many patients, particularly those with a multitude of additional cardiac pathologies and the elderly can be ineligible for catheter ablation.

High-dose radiation administered in one, or a small number of treatment sessions could produce tissue lesions similar to those of catheter ablation that prevent electrical conduction. This approach, cardiac radiosurgery, has been investigated in a number of animal studies. At present, these studies have either not compensated for the complex respiratory and cardiac contractile motion of the target area or have implanted fiducial markers for motion compensation. When no motion compensation is used, organs adjacent to treatment target are subjected to unacceptable radiation doses. More recently, cardiac radiosurgery techniques have been used in two humans for the treatment of ventricular tachycardia (VT). These studies also required implanted markers for motion compensation. If the desired non-invasive treatment of AF is to be achieved with radiosurgery a real-time motion compensation strategy without implanted markers is required.

Magnetic resonance imaging (MRI) is an advantageous imaging modality on account of its

non-invasive nature, lack of imaging dose and high image contrast of soft tissue structures. MRI has been utilised to follow three-dimensional target motion in the lungs, liver and kidneys. In very recent times, a non-invasive real-time motion compensation strategy to track the LA for has been developed with MRI. However, the limited capabilities of four-dimensional MRI has restricted its accuracy from being discerned.

This thesis focuses on quantification and development of the existing cardiac tracking method within a digitally simulated environment. The real-time motion compensation is ultimately designed to provide image-guided treatment of AF with an integrated MRI linear accelerator (MRI-Linac). Initially, a reverse engineering of the tracking algorithm was conducted on a perfect digital scenario. Investigation and confirmation of the general tracking functionality at this level then allowed a realistically simulated MRI workflow to be administered on a virtual patient cohort. Here, general tracking accuracy and patients' anatomical parameters' effect on the tracking are quantified. Finally, the newly developed function's performance on real-world data is qualitatively assessed.

Chapter 2 explores the physiology of AF and current treatment techniques. An extensive overview of the recently developed real-time LA tracking method is then provided to highlight its importance in the overall non-invasive radiosurgery treatment. Until now, the tracking remained unquantified hence chapter 2 concludes with a thorough description of the powerful simulation software that is utilised for this purpose.

The methodology behind providing a quantitative measure of a target's absolute motion is provided in chapter 3. Section one will explore the generation of a highly detailed, and thus unrealistic digital environment which allowed development of a multitude of new tracking functionalities. The optimised tracking methods are applied to a realistically simulated virtual patient scenario in section two, providing tracking measures which would resemble those seen in a real-world procedure. The justification behind a virtual patient's individual anatomy and physiology is further described in section two. The final section details moving away from a digital environment and how re-implementation of real-world MRI data is achieved.

Chapter 4 presents the accuracy results from the developed tracking functions described in the methodology chapter. It will detail patient specific physiologies that influence tracking accuracy and their correlations. Finally, the best performing tracking function combination implemented on real-world MRI data is assessed.

A comprehensive discussion of the previous chapter's results will be conducted in chapter 5. Their place in the larger context of the proposed MRI-guided radiosurgery is examined. The limitations of the project's individual components will also be discussed. Finally, recommendations for immediate areas of research and development for the proposed treatment of AF are put forward.

2

BACKGROUND

2.1 Atrial fibrillation

Atrial fibrillation (AF) is the most common and clinically significant cardiac arrhythmia. Presence of the condition is a strong risk factor of ischaemic stroke [25], increasing up to nearly five times with age [78]. The lifetime risk of developing AF for men and women over the age of 40 is approximately 1 in 4 [43], accentuating the burden AF has on the health system. Lower estimates suggest that over five and a half million Americans [25] will have AF by the year 2050 while Miyasaka *et al.* [50] reports this number may be as high as 15.9 million. Benjamin *et al.* [5] suggests the presence of AF alone is associated with a mortality risk factor of 1.9 and 1.5 for men and women, respectively. With over 10% of global deaths due solely to stroke [48], the underlying causes such as AF need to be thoroughly understood.

2.1.1 Atrial fibrillation physiology

AF can broadly be described as the result of ectopic electrical activity in the heart's two upper chambers, the atria (Fig.2.1), causing them to irregularly contract or "quiver". The ineffectual blood flow in the atria of an AF patient, resulting from the fibrillation can cause the blood to clot. Blood clots reaching the brain and blocking vascular structures can induce ischaemic strokes. Ventricular rates during a period of AF may reach 100 to 175 bpm with atrial rates reaching 200 - 400 bpm [51]. Problems related to such high heart rates are in addition to heart rhythm complications which are of equal concern [79]. The difference between normal sinus rhythm and that of AF is detailed in Fig.2.1.

Numerous pathophysiological processes in the heart's atria can give rise to AF [61]. These can be caused by chronic atrial stretch due to structural heart disease, neurohumoral activation (increased activity of the sympathetic nervous system) and aging. Characteristic

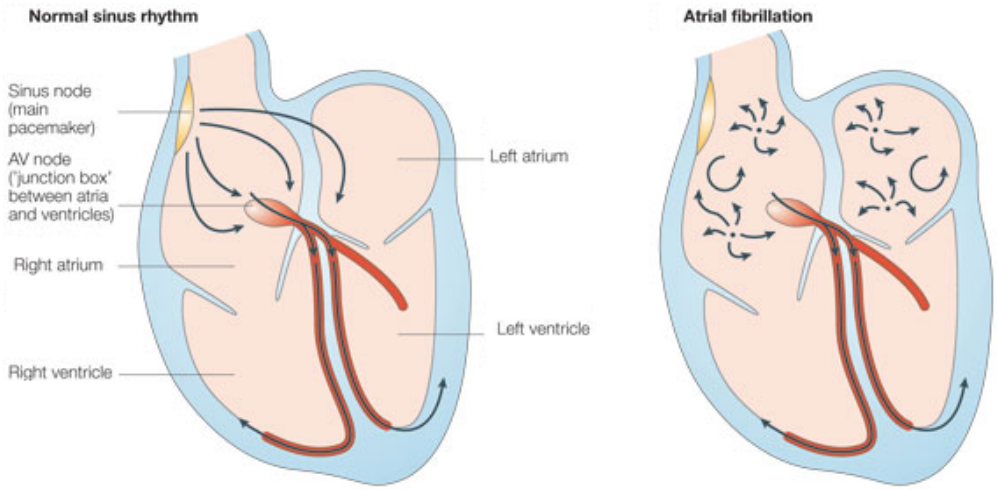

Fig. 2.1 (Left) Normal sinus rhythm. An electrical impulse originates in the sinus node, causing atrial contraction before being slowed through the AV node, upon entering the ventricles, where it causes ventricular contraction. (Right) AF electrical activity. Uncoordinated electrical activity in the atria caused by re-entrant wandering electrical wavelets. Adapted from [55].

electrophysiological properties of atria that present with AF can be shortened atrial refractory periods and disruption of electrical connections between muscle bundles [61]. Under these conditions, aberrant electrical signals from the pulmonary veins (PV) are more likely to enter the atria and form re-entrant circuits of electrical activation, triggering episodes of AF. When AF is diagnosed, its classification is dependent on its presentation and duration. The various subtypes are shown in Tab.2.1.

Table 2.1 Subtype and classification criteria for atrial fibrillation (AF).

Subtype	**Classification criteria**
First episode	*Initial detection, regardless of symptoms or duration*
Recurrent	*More than two episodes*
Paroxysmal	*Self terminating episode less than seven days in length*
Persistent	*More than seven days in length and non-self-terminating*
Long-standing persistent	*Persistent AF lasting more than one year*
Permanent	*Present for more than one year with unsuccessful rhythm control strategies*

Electrocardiogram

An electrocardiogram (ECG) is used to detect electrical signals of cardiac structures and is also used as a tool diagnosing AF against other heart disorders such as atrial flutter. Cardiac phase information can be determined from the ECG signal. P waves represent atrial systole while the QRS complex represents ventricular contraction. The R-wave is the most distinct feature of an ECG and is used extensively in this work as a triggering event in the tracking methodology. Fig.2.2 details an ECG of normally functioning sinus rhythm and an example AF signal. According to the Task Force for the Management of Atrial Fibrillation of the European Society of Cardiology [15] a patient's surface ECG must show "absolutely" irregular R-R intervals and there must be no distinct P waves on the surface ECG to be defined AF. However, some apparently normal atrial activity such as P wave imitation may be seen in some ECG leads. Additionally, an ECG of an AF patient may exhibit the absence of an isoelectric baseline, varying ventricular rates and fibrillatory waves small or large in amplitude.

2.1.2 Atrial fibrillation treatment

The reduction of stroke risk is the primary goal in the treatment of AF but reassertion towards a normal heart rate and heart rhythm is also vital. Medication is often used as a first line approach to achieve both of these treatment goals. The stroke risk can be lowered through anticoagulation medicines such as warfarin [11]. Restoration of a normal heart rate is mainly achieved by medication to slow the heartbeat such as beta-blockers whilst amiodarone can be used for sinus rhythm restoration [79]. In the event where heart control medications are ineffective and in some cases also as a first-line treatment for paroxysmal AF, catheter ablation surgery is considered as a treatment to relieve symptoms and improve quality of life.

Catheter ablation

Catheter ablation has been utilised in the treatment of heart rhythm disorders for more than 30 years and in the treatment of AF since 1998 [29]. In the treatment of AF a thin flexible tube known as a catheter is inserted into an inferior vein from the heart, usually near the groin and guided fluoroscopically through the vascular network to the treatment target, the PV antra of the left atrium (LA). Radiofrequency (RF) electrical current is applied through the catheter to produce small burn lesions approximately 6 to 8 mm in diameter. The multitude of electrical triggering and re-entrant sites shown to be present in AF patients [28] has resulted in treatment approaches where the catheter is moved from location to location to achieve complete electrical isolation between the LA and PV through many lesions, shown in Fig.2.3. The electrical conditions causing AF have been shown to vary between patients

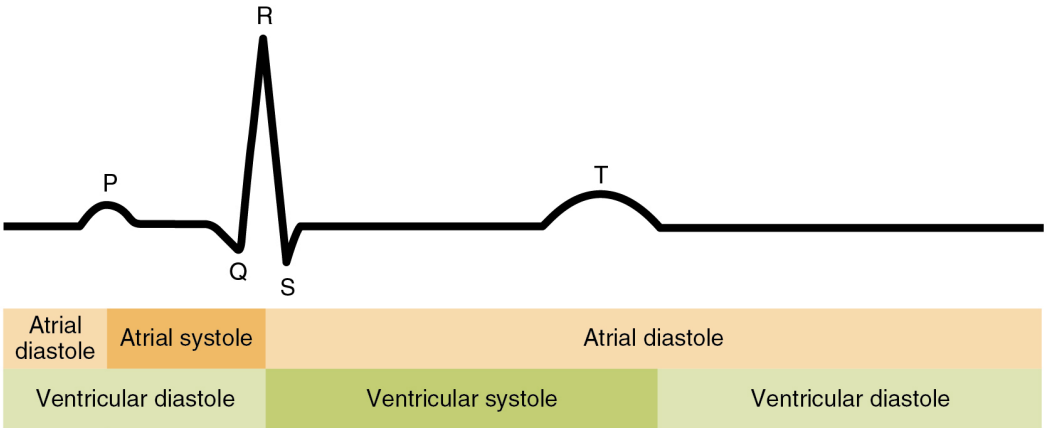

(a) An ECG signal of healthy sinus rhythm, with associated temporal chamber contractions (systole), or expansions (diastole). The P wave represents depolarisation of the atria and is followed by atrial systole. Atrial systole extends until the QRS complex, at which point, the atria relax. Adapted from [71].

(b) ECG signal of an AF example. No distinct P waves are visible and irregular R-R intervals are present. Adapted from [18].

Fig. 2.2 An ECG signal of healthy sinus rhythm and an example AF signal, highlighting characteristic components.

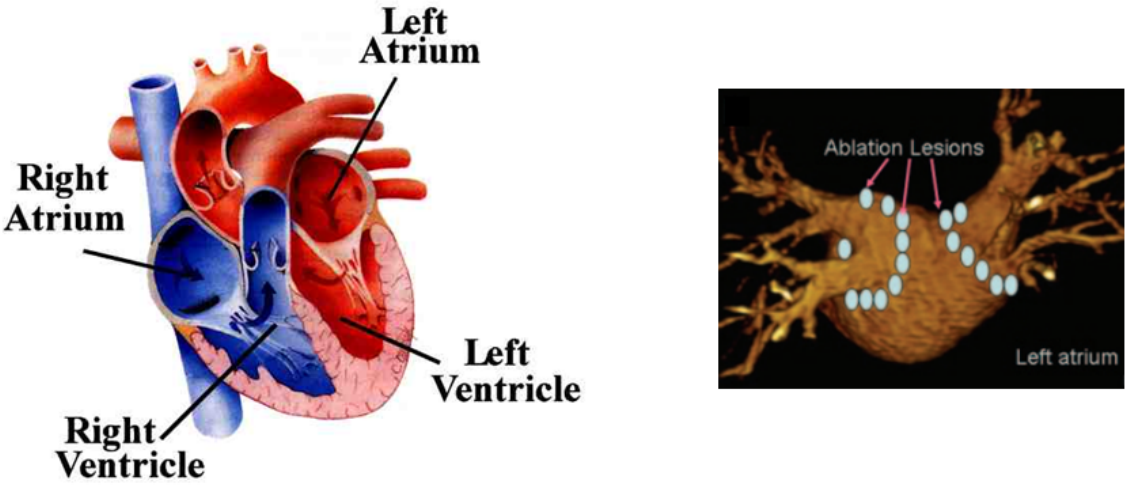

Fig. 2.3 (Left) Anterior cross-sectional view of human heart. (Right) Posterior view of the LA showing prescribed catheter induced lesions for the electrical isolation of the PV. Adapted from [2, 30].

and as a result, ablation procedures are often patient specific. Success of the surgery is often assessed with voltage mapping conducted after or during the procedure although a recent study conducted by Badger *et al.* [3] employed magnetic resonance imaging (MRI) as an evaluative tool of ablated lesions.

The LA volume has been shown to be a predictor of the outcome of catheter ablation surgery in the treatment of AF [1, 31]. Both studies associate successful PV isolation and a lack of AF recurrence with smaller LA volumes. Abecasis *et al.* [1] found a diastolic LA volume of 145 ml as a good cut-off value for AF recurrence after catheter ablation. Hof *et al.* [31] achieved complete success in only 28% of their patients with a diastolic LA volume over 150 ml. Patients with AF [1, 31, 70] and other cardiac pathologies [37] show larger LA volumes than those of normally functioning hearts [33].

The catheter ablation procedure has success rates of 30% to 90% in maintaining sinus rhythm over the following year [2]. Lower success rates are associated with the more developed AF subtypes while patients with AF subtypes that present intermission periods (see Tab.2.1) have the higher success rates. A 4.5% complication rate [16] and a 1% to 2% risk of developing a major, life-threatening complication [2] highlights the inherent physical risk of catheter ablation surgery. Ablation can damage the oesophagus, located behind the LA, leading to fatal bleeding or stroke after several days. Paralysis of the diaphragm can

occur from damage to the phrenic nerve, causing shortness of breath. AF catheter ablation logistically demands a highly skilled specialist, long treatment times of approximately four hours, specialised equipment and additional medicines such as anaesthesia and anticoagulants. Elderly patients with impairment of systolic function and those with inability to tolerate an invasive and time consuming procedure are generally ineligible for catheter ablation.

2.2 Towards MRI-guided cardiac radiosurgery

2.2.1 Radiosurgery

Since its early beginnings in the 1950s, stereotactic ablative radiosurgery (SABR) has become a standard of care and treatment in the management of cranial and extracranial conditions. Radiosurgery, like radiotherapy, is primarily used in the treatment of cancers [20] however in radiosurgery a high dose of radiation is administered in a single, or small number of fractions. This is in contrast to the increased fractionation schemes typically seen in conventional radiotherapy where healthy tissue is given time to repair radiation damage, a property that is exploited on account of its limited ability in cancerous cells. The term "stereotactic" refers to the coordinate system that allows correlation between a patient's pre-treatment imaging and the actual target's location within the patient. The stereotactic method was pioneered by Robert Clarke and Victor Horsley [66].

The first radiosurgical device "Gamma Knife I" was installed in Stockholm in 1967 with a cobalt-60 radiation source regime. The device had been designed to treat functional disorders but was also used in the treatment of malignant and benign cancers, and abnormally formed vascular structures [40]. Since its conception, the Gamma Knife models (Fig.2.4) have been through a multitude of redesign and modification iterations culminating in the most recent gamma unit, Perfexion, released by Elekta in 2007. In China the GammaStar medical group has had notable internal success with its gamma unit's abundance. The design is based on the Gamma Knife and used for cranial and extracranial radiosurgical applications.

Despite the heavy usage of linear accelerators (linacs) in radiotherapy during the 1990s their use in radiosurgery remained controversial with concerns around the accuracy of treatment delivery, related to moving parts not present on gamma units. Treatment delivery in radiosurgery must be extremely precise on account of the high doses administered in a small number of fractions. Several linac devices (CyberKnife, 600SR, Mitsubishi C-arm Linac,

Fig. 2.4 The GammaKnife Perfexion system, a stereotactic frame is secured to patient's head during procedure for treatment accuracy.

Fig. 2.5 The Novalis Tx system, equipped with Varian's RapidArc radiotherapy technology to simultaneously modulate aperture shape, dose rate, and gantry speed at every angle.

Fig. 2.6 The CyberKnife system, utilising the Synchrony guidance system for determining target position from breathing motion.

Novalis) for the sole purpose of radiosurgical applications were developed in part to respond to this concern. Fig.2.5 and Fig.2.6 show the Novalis and CyberKnife systems. The CyberKnife received approval from the Food and Drug Administration (FDA) in 2001 to treat any location in the body. Its submillimetre accuracy, demonstrated through anthropomorphic phantoms [17, 80] has allowed the CyberKnife to be used in cranial and extracranial stereotactic treatments.

2.2.2 Cardiac radiosurgery

The treatment of the heart with radiosurgery has been increasing in prominence over the last few years. The first cardiac radiosurgery treatments occurred in porcine models and have demonstrated the creation of cardiac lesions without serious complications [65] in addition to a successful AF imitation treatment [47]. Both of these studies made use of the CyberKnife system. In an effort to discern the dose required to create the desired transmural scarring Bode *et al.* [9] conducted electrophysiological mapping in the LA and upper right PV after a dose escalation study study ranging from 22.5 to 40 Gy, delivered to the target vein antrum, in eight mini-pigs. They found that doses greater than 30 Gy result in the circular scarring of targeted PV musculature. A similar dose escalation study conducted by Blanck *et al.* [7] to determine the minimum dose threshold for cardiac radiosurgery proposed doses of 32.5 Gy to 35 Gy would be required to achieve the desired electrical isolation.

More recently, SABR techniques have been used in human patients for the first time. Loo *et al.* [44] report on the first-in-human treatment of ventricular tachycardia (VT), a cardiac

arrhythmia, using stereotactic arrhythmia radioablation (STAR). The procedure resulted in no definite acute complications and a significant reduction in VT episodes, no sedative medications were required. Important to note is that the procedure did require a pacing wire to be fluoroscopically placed in the right ventricle as an imaging fiducial marker. In an additional single patient human study for the treatment of VT [19] a 25 Gy single fraction dose was applied using the CyberKnife system and in the follow-up period of six months no signs of toxicity or VT episodes were detected. However, like the previous study, invasive fiducial markers were required to correlate the breathing signal with target motion.

2.2.3 Guided radiosurgery

Image-guidance is a prerequisite for today's extracranial SABR procedures. Initially, radiosurgery was exclusively used for cranial applications. Outside of the skull, targets cannot easily be fixated, which is why there is a strong need for guidance. SABR guidance techniques that have been used on the CyberKnife and Novalis systems have incorporated orthogonal kV localisation techniques and kV cone-beam computed tomography (CT) localisation [8].

Recent advances in MRI target tracking [12], the lack of invasive fiducial markers [35] and its compatibility with audio-visual biofeedback to improve target tracking accuracy [41] has put forward the case for MRI guidance strategies. Combined with the intrinsic properties of MRI (no additional imaging dose, an unprecedented image contrast of soft tissue, functional imaging capabilities) the potential superiority of MRI in radiosurgical applications is apparent, especially with the advent of MRI-Linac technology.

2.2.4 MRI-Linac

The first linac-based system for MR-guided radiotherapy was installed in Utrecht, Netherlands [39], in 2014 and has been followed by programs in Edmonton, Canada [22], Toronto, Canada [36] and Sydney, Australia [38], where this project is based. The fusion of an MRI and a linac is no simple engineering problem with considerations required in linac construction, such as the electron gun [76]; relative linac proximity to the MRI magnetic fields; and how the radiation beams interact with these fields. The Australian MRI-Linac (Fig.2.7) program currently employs a temporary 1.5 T magnet and has recently administered its first beam on images. The final configuration plan is a specifically designed 1-T open-bore/6-MV linac system. The field is rapidly advancing with the goal of developing next generation cancer therapy equipment, in which changing patient anatomy

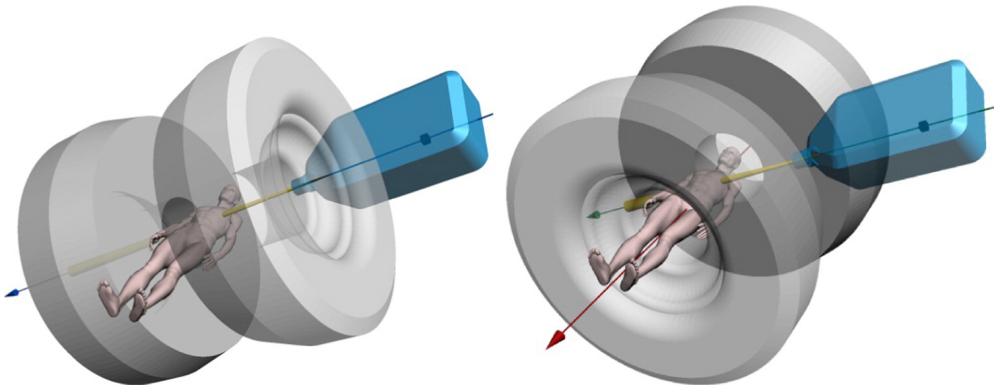

Fig. 2.7 Visualisation of the Australian MRI-Linac showing both orientations to be experimentally investigated. (Left) Inline orientation, linac aligned with B_0. (Right) Perpendicular orientation, linac perpendicular to B_0 [38].

and physiology can be visualised during treatment. The accuracy of treatment for cancer radiotherapy and cardiac radiosurgery holds great potential to directly improve patient treatment outcomes.

2.3 Foundation study

The purpose of this section is to summarise the initial cardiac research and developed tracking methodology conducted and published by Ipsen *et al.* [35] with the Radiation Physics Laboratory at the University of Sydney. In order to comprehend the extensions that have been made to the overall project, in this work, it is necessary to understand the foundation of the MRI cardiac tracking methodology. To account for the lack of 4D MRI data and the complex geometrical behaviour of the LA through respiratory and cardiac cycles, a template matching method was developed. The methodology along with necessary background is described in the following subsections

2.3.1 Treatment planning

Treatment plans with targets adapted from catheter ablation surgery (Fig.2.3) were generated for differing planning target volume (PTV) margin sizes (0, 1, 3, 5 and 8 mm) on a single patient's cardiac gated CT scan. The patient was to receive catheter ablation surgery for the treatment of AF [35]. The organ at risk (OAR) dose resulting from the 30 Gy single-fraction radiosurgery treatment was analysed for the various margin sizes. They concluded that most dose limitations could be met if margins were kept below 5 mm (Fig.2.8), although doses to the heart necessarily exceeded the acceptable limits of RTOG 0915 in all treatment plans.

Subvolume regions of the heart subjected to dose over the 22 Gy RTOG 0915 acceptable limit were observed.

The treatment target for the proposed radiosurgery, the PV antra, experience complex respiratory and contractile motion components, shown to be up to 29.7 mm (SI plane) and 3.3 mm [34]. For target motion trajectories of this magnitude and on account of the treatment planning study results it is clear that an alternate motion compensation strategy is required in order to maintain small margin size and reduce the dose to the heart and surrounding OARs. The MRI-Linac system provides real-time image data and allows direct feedback to either pause the treatment temporarily or to update the treatment beam position with a multi-leaf collimator (MLC). This functionality enables two motion compensation strategies to be considered: gating and target tracking with real-time MRI. A gated treatment scenario would see an increase in the procedure time and may require additional equipment to provide a respiratory signal. Both are features that a tracking with real-time MRI approach would not require. Combined with recent successes in 4D organ tracking that utilise real-time 2D MRI images [6, 12, 69] the developed LA tracking method is a promising motion compensation strategy for the proposed treatment of AF with the MRI-Linac system.

2.3.2 3D MRI cardiac tracking

The real-time tracking developed by Ipsen [34] focuses on the optimisation of a template matching tracking approach for the proposed cardiac application. In an effort to track organs such as the liver [12] and kidneys [6] with MRI, template matching approaches have been investigated but have taken organs as rigid shapes that move only as a result of diaphragmatic respiratory motion. In the case of tracking the LA it is infeasible to assume rigidity on account of the cardiac contractile motion, accordingly, a dual template matching method supported by an ECG surrogate signal was implemented. The cardiac tracking workflow is shown in Fig.2.9 and outlined in the following paragraphs.

Pre-treatment imaging

The LA is traversed sagittally with cine MRI, short movies of average myocardium motion and blood flow throughout the cardiac cycle, with patients holding their breath at end-exhale with the following parameters: True fast imaging with steady state precession (TrueFISP), echo time (TE)/repetition time (TR) = 1.5/41.5 ms, pixel spacing = 1.3 mm^2, field-of-view (FOV) = 282 mm^2, slice thickness = 5 mm. The volumetric centre of the LA is visually assessed and positioned at the MRI scanner centre coordinate. The sagittal images are retrospectively gated to ten cardiac phases and sorted into corresponding cardiac phase

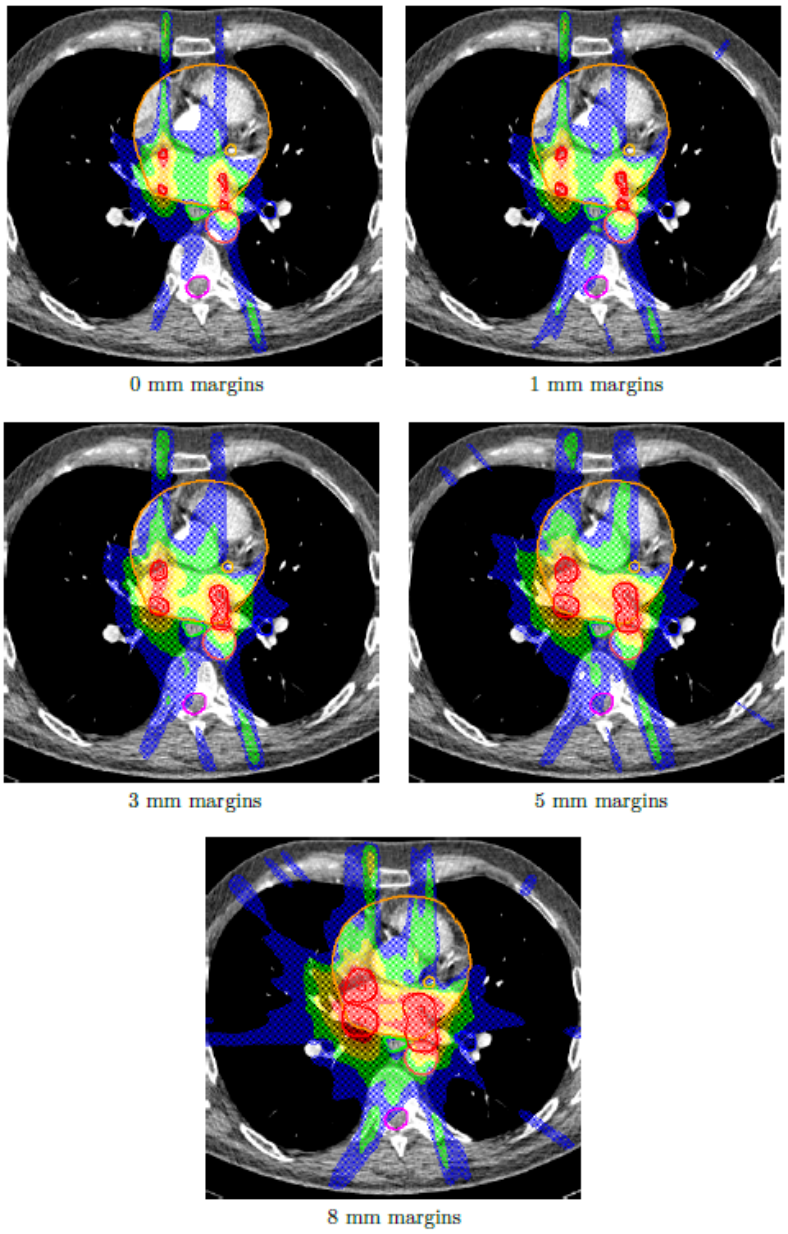

Fig. 2.8 Resultant dose distributions for different margin sizes. Red $\geq$ 30 Gy, orange $\geq$ 25 Gy, yellow $\geq$ 20 Gy, green $\geq$ 15 Gy, blue $\geq$ 10 Gy. From Ipsen [34].

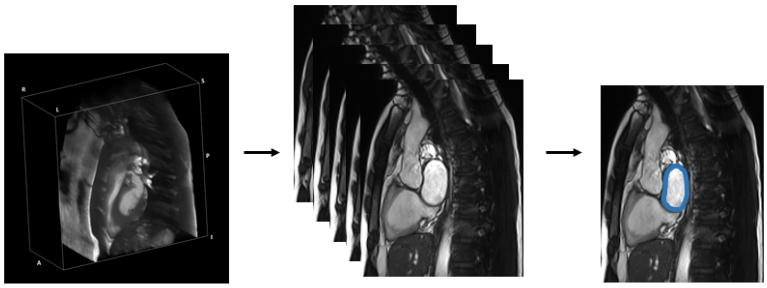

(a) **Pre-treatment imaging.** 3D volume (left) comprised of sagittal slices (middle) spanning the LA's LR length. The LA is manually delineated in each frame (right) to form the 3D template, repeated for systole and diastole phases.

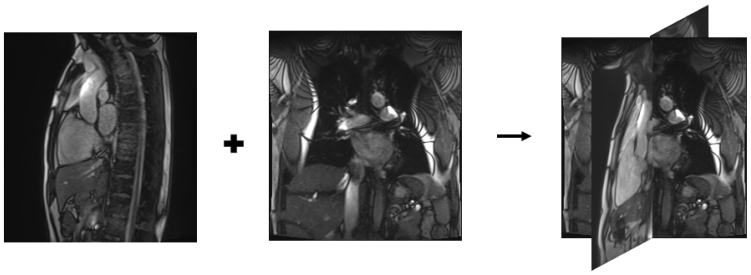

(b) **2D real-time MRI.** Orthogonal interleaved planes (right) are acquired sag (left) then cor (right) in real-time with corresponding ECG signal.

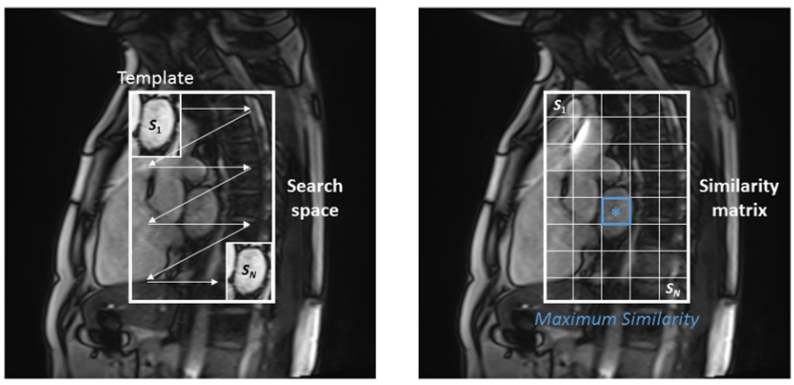

(c) **Real-time target localisation.** The 3D pre-treatment LA volume is successively moved over the real-time planes (left). Maximum similarity between the pre-treatment volume and real-time plane infers 4D target location (right). The ECG signal determines whether a systole or diastole template is used.

Fig. 2.9 The current workflow for the proposed real-time target localisation.

volumes. The volumes are then manually delineated slice-by-slice to extract the LA template volumes.

2D real-time MRI

The real-time sagittal and coronal orthogonal images are acquired in a free breathing environment with the following parameters: TrueFISP, TE/TR = 1.3-1.5/51-72 ms, pixel spacing = 2.0 mm^2, FOV = 326-370 mm^2, slice thickness = 6 mm, acquisition time = 200-252 ms. The point of intersection between the two image planes is required to be the volumetric centre of the LA and is accordingly set with the MRI scanner. Due to the nature of their anatomical orientation and anisotropic voxels, both planes produce high spatial detail in the superior inferior (SI) plane while coronal planes produce high spatial detail in the left right (LR) direction and sagittal planes produce high spatial detail in the anterior posterior (AP) direction.

Real-time target localisation

The pre-treatment systole or diastole volume template is selected from the ECG signal, binned based on the distinct R peak, and iterated over the real-time image where a similarity matrix is formed. The systole template is used for 30% of the cardiac cycle and the remaining 70% of the heart cycle is matched with a diastole template, based on documented heart rhythm [57]. A maximum-diastole/systole template combination proved more accurate in initial 2D experiments than an end-diastole/systole combination and was continued into the 3D scenario. The location of highest similarity between an individual template plane and the real-time plane is used as the coordinate basis to infer 4D positions about other anatomical areas in the template. Based on the results from Ipsen [34] a cosine measure proved to be the most accurate in 2D tracking experiments and was extended to the 3D tracking. The cosine measure between the target and real-time image pixels, here T and RT, is as follows:

$$COS = \frac{\sum_{i=1}^{n} T_{\mathrm{i}} \;\; x \;\; RT_{\mathrm{i}}}{\sqrt{\sum_{i=1}^{n} T_i^2} \;\; x \;\; \sqrt{\sum_{i=1}^{n} RT_i^2}}$$

Due to their respective superior in-plane resolutions, the coronal and sagittal real-time planes are used to infer the LR and AP locations. The target's AP location is updated on every sagittal slice while the target's LR location is updated on every coronal slice. As a result of the orthogonal interleaved nature, the SI position is updated every slice while the AP and LR information is updated every second slice. The importance of this is demonstrated in Ipsen *et al.* [35] where the highest motion magnitude of the LA was found in the SI plane in a free breathing scenario while significantly less motion was measured in AP and LR. The last

slice's matched AP or LR location instructs the tracking algorithm of which current template slice to perform matching with.

2.3.3 Limitations

Ideally tracking would utilise real-time 4D MRI data as opposed to the 2D-2D orthogonal planes. This is not yet possible in MRI due to long acquisition times, reconstruction times, and somewhat limited spatial resolution needed to analyse the fine movement of the cardiac system.

When matching the current slice, its position is based off the last best match location. In order for this systematic process to be accurate the initial condition of template and real-time LA volumetric centres coinciding with the scanner coordinate isocentre must be set up. This can be difficult to achieve in practice in a real-world environment.

Additionally, the LR and AP target positions being updated every second slice results in a loss of information for these directions. Acquisition times of 200 to 252 ms in addition to computation times imply that over half of a normally beating heart cycle may transpire before the position is updated again. A faster beating heart is expected to accentuate the issue.

A dual template method, while superior to a single template approach, is associated with corresponding errors. The introduction of a dual template method seeks to reduce the tracking to respiratory motion only, by incorporating the cardiac contraction in the template volumes. The cardiac contraction of the PV antra between systole and end-diastole has been shown to be averaged at 1.8 mm for the right PV and 1.5 mm for the left PV [34] across studied patients, a value which is unaccounted for in this tracking method due to end-diastolic treatment planning.

Perhaps the biggest limiting factor of the work conducted by Ipsen [34] is the lack of a "ground truth", due to the unavailability of real-time 4D MRI data. Ideally, MRI would allow real-time 4D data appropriate for this application. While the individual 2D tracking has been quantified with a mean error of 3.0 mm [34] this has yet to be evaluated on the 3D approach.

This thesis focuses on quantifying, analysing and advancing the original cardiac tracking work which has been developed for a non-invasive radiosurgical treatment of AF with the MRI-Linac. The 4 dimensional extended cardiac-torso (XCAT) phantom is used as a

quantitative tool to test the standing method and quantify improvement during the development of different and novel approaches, before subjecting a virtual patient dataset to the tracking methodology. Finally, the changes and adaptations are applied to real cardiac MRI volunteer scans to qualitatively assess the developed and improved methods.

2.4 4D extended cardiac-torso phantom

The XCAT phantom is a digital phantom platform that simulates realistic anthropomorphic anatomy and physiology. The XCAT phantom is needed to test the LA tracking methods that are being developed due to the unavailability of 4D MRI data. The XCAT phantom was developed for medical imaging research, pliable to a range of imaging modalities [62] and is a desirable tool for exploring and developing the cardiac tracking methodology.

The XCAT phantom has been used periodically in experimental investigations as a tool for verification and as a proof of concept for imaging simulations and image interpretation strategies. Tobon *et al.* [68] generated a group of 40 virtual subjects using the XCAT phantom with the goal of producing realistic simulation of cardiac MRI. Veress *et al.* [74] employed the XCAT in conjunction with a finite-element (FE) model to more accurately simulate regional heart defects caused by ischaemia. The XCAT phantom was also used to assess an innovative 4D-MRI technique which utilises the body area of axial MR images as a respiratory surrogate for a breathing signal [14]. Finally, a novel respiration-phase-matched digital tomosynthesis technique to monitor moving targets was verified with the XCAT phantom [81]. The XCAT phantom's realistic and quantifiable cardiac 4D geometries in addition to its recent use in MRI simulation and image analysis techniques reinforces its aptitude for developing the cardiac tracking methodology introduced in Sec.2.3.2.

2.4.1 XCAT overview

The XCAT's anatomy development, its 4D interactions and how it can be used to simulate medical imaging is described in the following paragraphs. The 3D anatomical properties of the XCAT phantom are based on the Visible Human data from the United States' National Library of Medicine. Only the cardiac and brain models of the XCAT are not derived from this data set. The brain model is developed from 3D MRI data while the XCAT cardiac model is modelled from 4D gated multislice computed tomography (MSCT) data. On account of its relevance, only the cardiac model is further described in Sec.2.4.2.

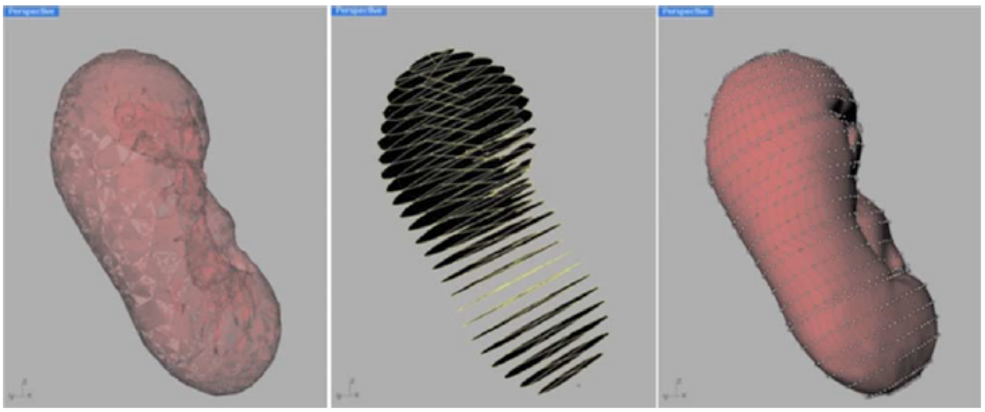

Fig. 2.10 Modelling of the XCAT kidney. (Left) Showing the polygon segmented mesh. (Middle) Contours taken from polygon mesh. (Right) 3D NURBS surface is fitted [62].

The anatomical images from the Visible Male dataset are taken from axial CT slices with an in-plane resolution of 2048 by 1216 pixels spaced at 0.33 mm and 1 mm slice thickness [53]. This spatial resolution is superior to traditional CT datasets which are typically of 3-5 mm slice thickness [62]. The developers of the XCAT phantom segmented anatomical structures using custom software, creating 3D polygon models. Interpolation using cubic spline surfaces allowed for faster creation of these models. A 3D non-uniform rational basis spline (NURBS) surface is then fitted to the anatomical polygon structures. An example of this process for the XCAT kidney is shown in Fig.2.10.

A NURBS surface is a mathematical model used for generating and representing curves, surfaces and ultimately complex shapes. A NURBS surface is superior to a polygon mesh in that its points are connected by spline curves and require only a few control points to define a surface, whereas a polygon mesh requires many points to define a smooth surface. Fig.2.11 shows how a NURBS surface's shape can be modified by manipulating one of its control points and the corresponding result if conducted on a polygon mesh.

The respiratory motion model of the XCAT phantom is controlled by two time curves, the first controlling the diaphragmatic height and the second controlling the AP expansion of the chest. The AP curve controls the rib cage's outward and upward chest expansion and the diaphragm's forward motion. The diaphragmatic curve controls the downward contraction of the diaphragm. The liver, stomach, spleen and kidneys all move with reduced and scaled motion based on the diaphragm motion. The remaining structures that move due to respiration (muscle tissue, organ vessels and abdominal organs) are controlled by a motion vector field that is determined off the primary organ motions previously described. Motion

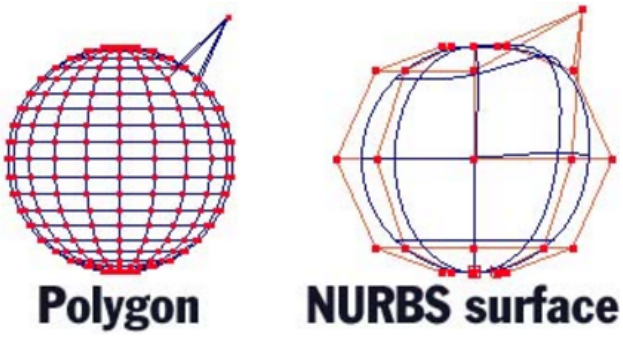

Fig. 2.11 Illustration of the number of control points needed for a polygon mesh and a NURBS surface. Also depicts the resultant shape of a single control point manipulation [72].

vector trajectories of all organs and structures are checked to ensure no collisions, and once satisfied the motion vectors are applied to the NURBS control points which ultimately causes structure expansion and contraction over time. The XCAT phantom allows users to control breathing rate, magnitude of diaphragm motion and chest expansion. The heart's respiratory motion is unique in that it is not derived from diaphragmatic motion but is instead able to be controlled in all three anatomical planes, directly from user input with its own motion time curve [62].

The XCAT phantoms can generate attenuation models or activity models. These two physical models allow users to conduct multimodality imaging research. Both models are stored as a voxelised phantom of user defined resolution. The attenuation mode displays a 3D distribution of attenuation coefficients for a given photon energy, used in simulating x-ray, CT and emission imaging while the activity mode displays a 3D distribution of radionuclide emission activity for the XCAT's organs and allows users to simulate MRI by setting activities of XCAT anatomies to a specific imaging property, such as T1, T2 or proton density.

2.4.2 XCAT cardiac model

The 4D XCAT cardiac system is modelled from high-resolution cardiac-gated MSCT data from healthy male and female subjects. The advent of MSCT systems has allowed for a high level of detail in 4D cardiac imaging not previously available with single-slice CT systems. The reason for this improvement and main differentiating factor of the two systems is the detector array configuration, MSCT systems split the traditional z-axis detector row into a 2D array of smaller detector units [26].

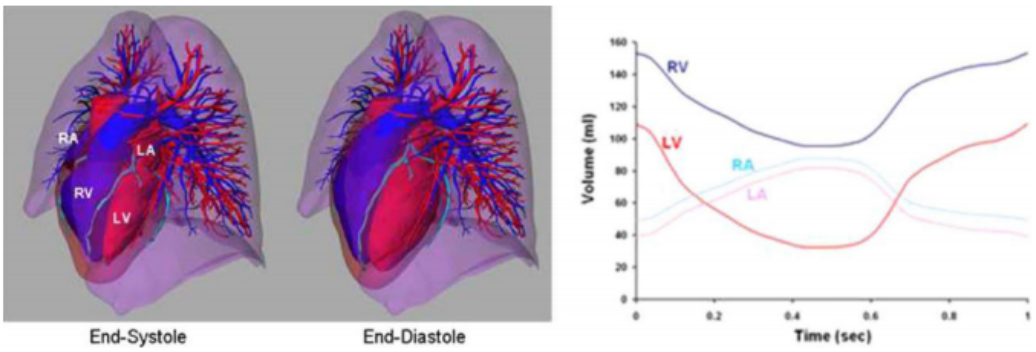

Fig. 2.12 (Left) 3D XCAT heart reconstruction at end-systole and end-diastole. (Right) Volume change over time of the LA and other chambers based off MSCT data [63].

The male XCAT cardiac model was developed from MSCT data that incorporated 100 time frames over a single heartbeat with in-plane pixel resolution of 0.32 mm^2, axially, and a slice thickness of 0.4 mm. The temporal detail was scaled down to 20 time points (every fifth frame) over the cardiac cycle for pragmatic purposes. The female dataset contained 12 time frames for a cardiac cycle with slice thicknesses of 0.6 mm. In-plane spatial resolution was consistent with the male dataset. The left and right ventricles and atria were segmented in each frame and converted to 3D polygon models in which 3D NURBS surfaces were fitted. The volume curve for the LA over time is shown along with the other three heart chambers in Fig.2.12.

The twisting and contraction motions of the heart are modeled from tagged MRI data collected by the developer of the XCAT phantom and show agreement with additional tagged MRI analysis [56]. Control-point specific time curves, providing positional information, create a 3D surface changing over time or a 4D NURBS model for each chamber, including the LA. Realistic NURBS surfaces for the heart chambers and coronary artery tree combined with the user determined input parameters that control the cardiac system allow for a range of heart beat trajectories, normal and pathological, to be modelled. The user defined input parameters which control the XCAT cardiac system are shown in Tab.2.2.

2.4.3 MRXCAT

An extension to the XCAT phantom was developed for cardiovascular magnetic resonance simulations, the MRXCAT [77]. Unfortunately, its cardiac short axis view, the assumed instant acquisition of image segments and lower user malleability made the MRXCAT inadequate as a quantitative tool in this work.

Table 2.2 4 dimensional extended cardiac-torso (XCAT) phantom cardiac motion and anatomical parameters, adapted from Segars *et al.* [62].

Anatomical and motion parameters	
Parameter	**Description**
X, Y and Z scaling of entire phantom	*One-dimensional scaling factors applied to entire phantom*
Heart scale	*Scales the heart in 3D*
X, Y, and Z translations and rotations for the heart	*Sets the position of the heart in the body*
Volume parameters for the organs	*Sets the volumes of the different organs*
Heart period	*Sets the length of the heart cycle*
Left ventricle volume parameters	*Sets the LV volumes at end-diastole, end-systole, at the beginning of the quiet phase, at the end the quiet phase, and during reduced filling*
Cardiac cycle timing parameters	*Sets the duration from end-diastole to end-systole, the duration from end-systole to the beginning of the quiet phase, the duration from the beginning to the end of the quiet phase, and the duration from the end of the quiet phase to reduced filling*
Heart respiratory motion translations	*Sets the x, y, and z extents in cm of the heart's motion during breathing*
Heart respiratory motion rotations	*Sets the extents in degrees of the x, y, and z rotations of the heart during breathing*

3

METHODS

If the end goal of magnetic resonance imaging (MRI)-guided radiosurgery with an integrated MRI linear accelerator (Linac) is to be achieved it must be demonstrated that tracking accuracy can be below the acceptable treatment margins discerned in Sec.2.3.1. The quantification of the established left atrium (LA) tracking method introduced in the previous chapter in addition to developed methods is the main goal of this thesis. Currently there is no quantitative measure of how well the tracking algorithm is performing. The 4 dimensional extended cardiac-torso (XCAT) digital phantom provides a powerful tool for this purpose.

Thorough understanding of the original tracking algorithm is the purpose of Sec.3.1 and is achieved by subjecting it to a best case digital scenario. The presence of a ground-truth allowed engineering fixes to be implemented and tested, leading to a more robust framework. Based on this, Sec.3.2 describes the development of new tracking functionalities which were tested on a virtual patient dataset modified to mimic real image data. Finally, the best performing tracking method was applied to real-world anatomical data for qualitative assessment in Sec.3.4.

3.1 Quantification of original tracking

Replication of the original LA tracking method (Sec.2.3.2) with the XCAT phantom required the generation of a phantom for every cardiac phase and for a free breathing scenario. Phantoms with high levels of spatial and temporal detail were generated for the initial analysis. This was due to the complexity of the existing tracking algorithm and the large number of associated uncertainties to be tested. Investigation and confirmation of the general tracking functionality at this high resolution then allowed degradation of the virtual data in a

second step (Sec.3.2) to model a real-world MRI environment - the major contribution to this work.

3.1.1 2D images for 3D template generation

The cardiac phase templates were generated from the default male XCAT phantom anatomies (Tab.3.1) with a 1 mm isotropic voxel size. The phantoms were subjected to beating heart motion only with complete elimination of the respiratory motion component to mimic an acquisition during breath-hold as was used in the original tracking study [35]. The cardiac cycle is binned into ten discrete cardiac phases. The 3D phantom is sorted into sagittal slices oriented right to left with the largest LA volume phase, maximum diastole determining the number of slices required to cover the entire LA for each template. The number of sagittal slices, i.e. the template width, is kept constant over all cardiac phases and additionally includes two 'empty' slices with no LA present on either side of the volume. This is to increase tracking robustness.

Digital Imaging and Communications in Medicine (DICOM) (see Sec.B) metadata is used as input in the cardiac tracking to ultimately give real-time positional information about the LA. The XCAT phantom does not produce metadata, consequently, DICOM header information and the previously described sagittal sorting were realised in MATLAB (The Mathworks Inc., US). The DICOM information is identical for all template phases and individual slices of a template differ only in slice location. The XCAT DICOM header information is generated so that the LA centre of mass is visually assessed to be at the MRI scanner coordinate isocentre (0,0,0). An example volumetric LA width before automatic LA template delineation template is shown in Fig.3.1. Following the phase sorting and isocentre alignment the LA templates were generated using automatic segmentation. The XCAT phantom produces homogeneous pixel values for each specified heart region, thus allowing for a simple pixel thresholding of the intended LA target. The automatic nature of the segmentation is advantageous in that no areas of the LA are missed and any inter-user variability is removed.

3.1.2 2D-2D real-time images

In the original tracking workflow, the 3D templates are being matched to orthogonal 2D real-time planes. Simulation of real-time images was conducted on the XCAT default male phantom parameters (Tab.3.1) in a free breathing environment. The phantom consisted of 100 time frames utilising 1 mm isotropic voxels. A temporal resolution of 100 ms to simulate the acquisition time per plane (interleaved acquisition sagittal-coronal-sagittal-...).

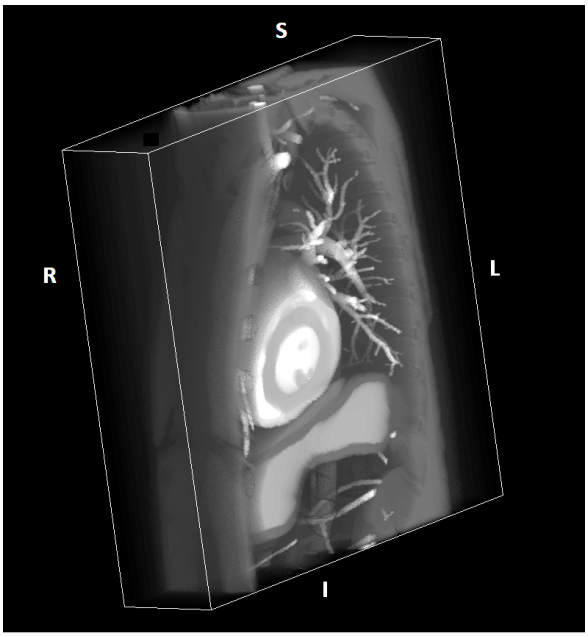

Fig. 3.1 The volume composed of XCAT maximum-diastole sagittal 2D slices spanning the width of the LA.

This is much higher temporal resolution than used by Ipsen *et al.* [35] and other true fast imaging with steady state precession (TrueFISP) tracking applications. [12, 54] However, giving more detailed information regarding the deformation and tracking of the LA this higher frame rate facilitated the analysis of the original tracking algorithm.

As a result, a single heart beat (mean duration $\sim$1000 ms at 60 bpm) is captured in ten individual real-time frames (five sagittal, five coronal). Using custom built MATLAB software the real-time phantom's interleaved frame sequence was realised by generating two types of raw data phantoms (sagittal and coronal orientation), extracting the middle slice as the real-time plane and adding the relevant DICOM header information. The real-time image's DICOM metadata information needed in the LA tracking is consistent with standard sagittal and coronal plane orientations, at successive times of acquisition.

The LA target localisation is extracted following the methodology described in Sec.2.3.2. The LA's centre position is defined as the centre coordinate of the sagittal-coronal plane intersection and is calculated from the DICOM information. On account of the volumetric LA template centre (Sec.3.1.1), and the real-time LA intersection both being defined at the scanner isocentre (0,0,0), any measured template shift in the real-time images can be inferred as the motion trajectory of the LA. If the measured template shift is intended to measure the

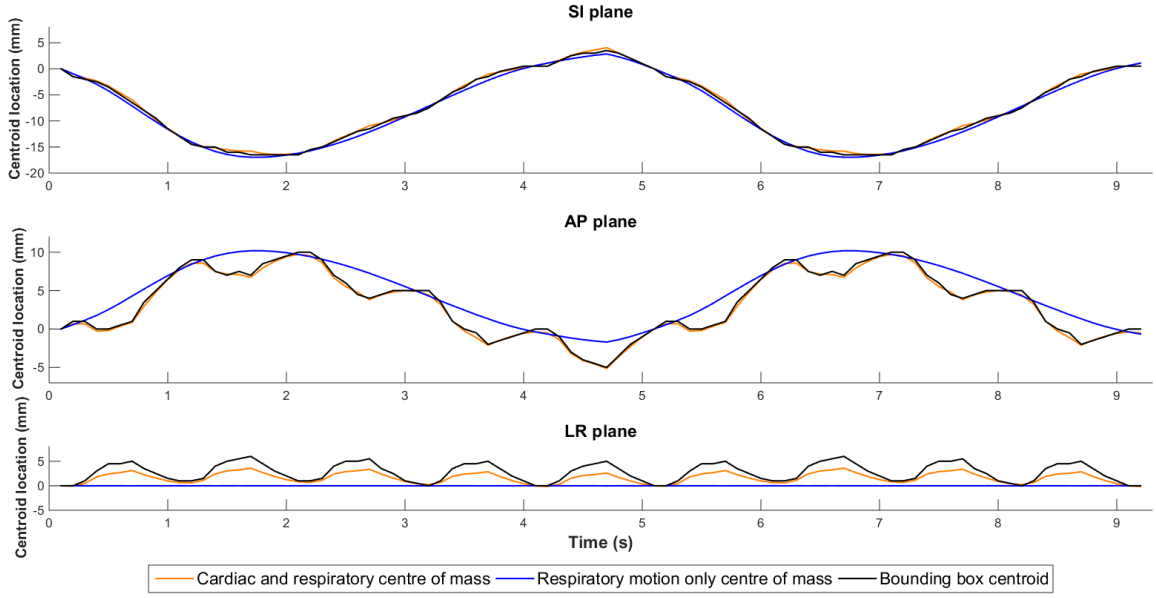

Fig. 3.2 Centroid location in the three anatomical planes for the three proposed quantitative measures for the default XCAT male phantom parameters.

absolute motion it is imperative that the 2D scans used for template generation and 2D-2D real-time images be centralised in this way. The current slice's AP/LR position is based off the best similarity match location of the last sagittal or coronal plane, respectively.

3.1.3 XCAT ground-truth motion

The XCAT ground-truth motion was first calculated in MATLAB using three different measures: an LA centre of mass location with normal cardiac contraction and respiratory motion; an LA centre of mass location for a static heart beat, only undergoing respiratory motion; and a centroid location of a bounding box surrounding the LA. Fig.3.2 illustrates the difference in these ground-truth centroid locations.

On account of the original tracking algorithm methodology described in Sec.2.3.2, the bounding box centroid was chosen as the ground-truth quantitative measure for the remainder of this work. The LA and the bounding box measure are visually represented in Fig.3.3. The centre coordinate of the bounding box is described as:

$$(SI_{\text{cent}}, AP_{\text{cent}}, LR_{\text{cent}},) = (SI_{\text{origin}} + \frac{SI\ length}{2},\ AP_{\text{origin}} + \frac{AP\ length}{2},\ LR_{\text{origin}} + \frac{LR\ length}{2})$$

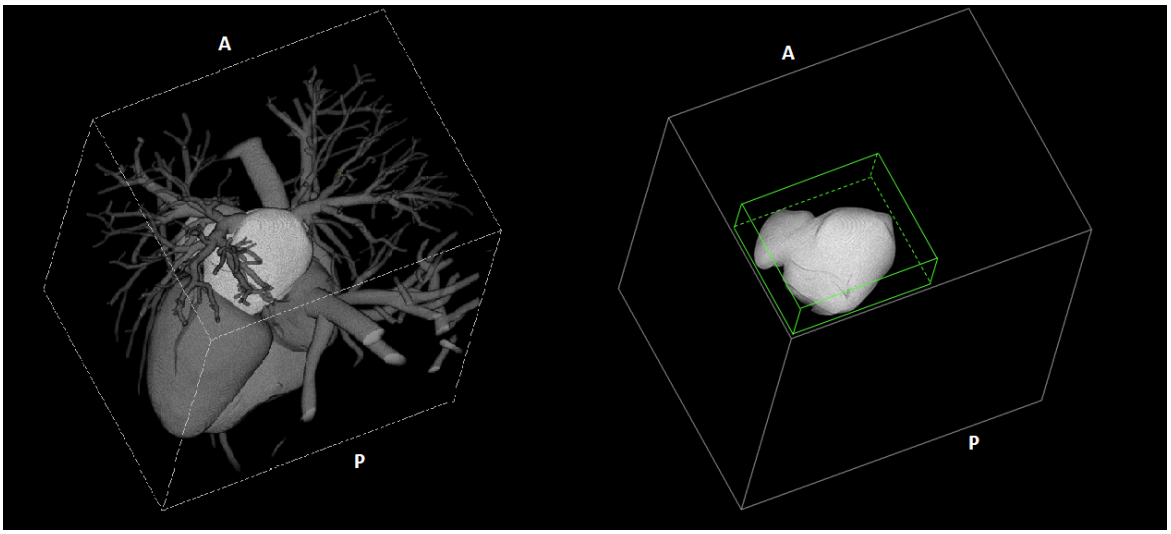

Fig. 3.3 (Left) 3D volume render of the XCAT cardiac model, lighter grey illustrating LA. (Right) Bounding box of LA, calculated in each time frame.

3.1.4 Absolute motion of template centres

The original tracking outputs the trajectories of the template's bounded box centre coordinate in three anatomical planes. While giving information on the relative shift for each template this method usually does not allow tracking of absolute motion of a specific region or the entire LA volumetrically over time. When multiple templates are used potential differences in template centre coordinates can occur. A correction function was written and added to the tracking functionality to output absolute target motion. The difference is highlighted in Fig.3.4. Comparison of an individual's absolute motion with the XCAT ground-truth motion using a root-mean-square (RMS) measure allows a quantitative analysis of the tracking algorithm's performance.

3.2 Virtual patient study

The aim of the virtual patient tracking study is to simulate the conditions of the LA tracking methodology with the XCAT phantom as closely as possible. The initial XCAT simulation introduced in the previous section (Sec.3.1) represents an ideal and thus unrealistic scenario but was a necessary step in the software development process because of the many tracking uncertainties initially untested. However, covering only a single patient's physiology and having a high image homogeneity, spatial resolution and temporal resolution led to a somewhat artificial image appearance and image plane parameters that current MRI technology would not ordinarily acquire. Therefore, the virtual patient study strives towards

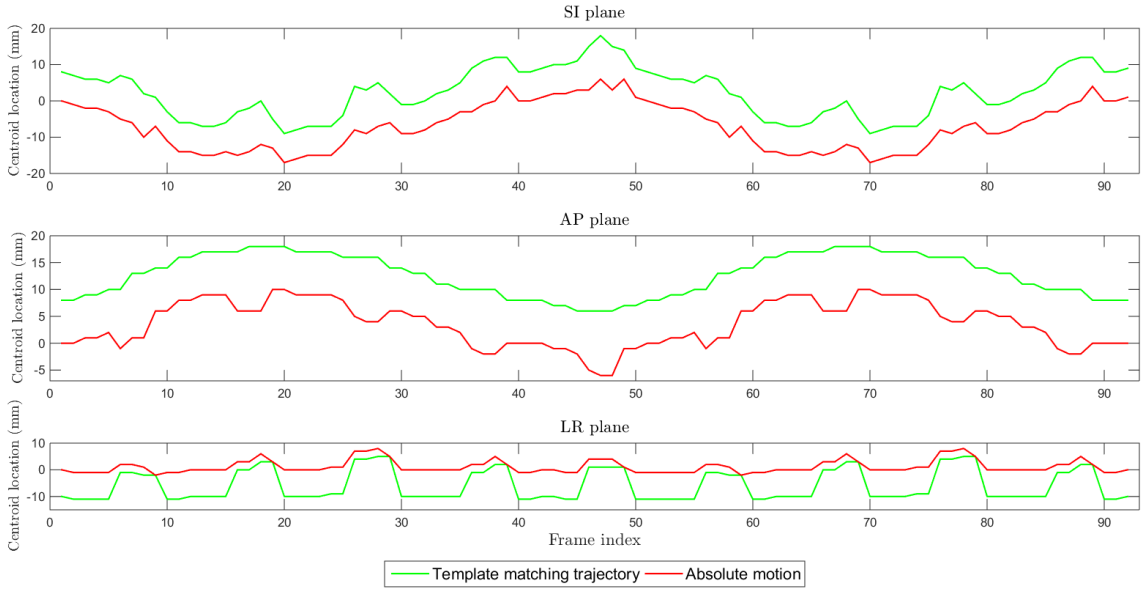

Fig. 3.4 Comparison of the template shift output against the implemented absolute motion correction. Using the default XCAT male phantom anatomies. Peaks and troughs in the corrected motion trajectories represent the periodic systolic phases.

a more realistic simulation that provides insight into how the LA tracking would perform for the general population and real anatomical data. The following sections describe how this was implemented.

3.2.1 Virtual patient anatomical and physiological parameters

To test, analyse and expand the cardiac tracking method the XCAT phantom's ability to control anatomical and physiological parameters was fully embraced to create a virtual dataset of 20 patients. Pixel intensities of anatomical structures in the virtual studies were modelled off the intensities extracted from volunteer MRI scans [34]. The LA volume, heart rate, respiratory rate and cardiac respiratory motion broken into its three constituent components (SI, AP, LR) were selected and varied across the 20 virtual patients. The three motion parameters (heart rate, respiratory rate, respiratory motion) are controlled directly in the XCAT phantom's parameter file while the LA volume is controlled indirectly by scaling the entire phantom or scaling the heart only. To date, only healthy volunteer patients have been assessed with the cardiac tracking method. Accordingly, the virtual dataset was designed to replicate this. The XCAT virtual patient parameters are shown in Tab.3.1.

The LA volume during maximum diastole was varied due to initial experimentation with the

cardiac tracking method indicating that object size and uniformity impact tracking accuracy. This is in addition to its prediction of successful catheter ablation surgery as described in Sec.2.1.2. The XCAT patient's maximal LA volumes were randomly generated with 103 ± 30 ml (mean ± SD) volumes, taken from cardiac MRI analysis of normal LA volumes as reported by Hudsmith *et al.* [33].

The virtual patients' LA respiratory motion were randomly generated based on the results of left atrial real-time motion assessment conducted by Ipsen [34]. Cardiac cine MRI of five healthy volunteers showed superior inferior (SI) motion of 16.5 ± 8.0 mm (mean ± SD), anterior posterior (AP) motion of 5.8 ± 3.5 mm (mean ± SD) and left right (LR) motion of 3.1 ± 1.1 mm (mean ± SD) between end-exhale and end-inhale. The range of motion between end-exhale and end-inhale is expected to cover the full extent of possible motions the LA may undergo during free breathing in the proposed radiosurgical procedure.

Heart rates from the seven healthy volunteer scanned to date (five volunteers from Ipsen [34] and two conducted as part of this work) were ascertained from ECG analysis to have an averaged 58.3 ± 10.3 bpm (mean ± SD). The virtual patient heart rates were randomly generated to model this distribution. Volunteer seven reported feeling nervous and presented a heart rate of 79 bpm. This heart rate was included due to similar heart rates likely being present in the proposed, more intensive radiosurgery procedure.

Finally, the virtual patients' respiration rates were randomly generated from normal human respiration rates of 13.5 ± 1.5 cycles per min (mean ± SD) as reported in Ganong *et al.* [23].

3.2.2 Virtual patient cardiac template images

The 2D scans for creating the 3D cardiac templates were replicated as closely as possible from the previous work [34] with the parameters shown in Tab.3.2. The scan parameters and the subsequent generation of the templates follow the methodology described in Sec.3.1.1 for the 1 mm isotropic phantom with changes only in the spatial resolutions and an added image artefact.

Inclusion of partial volume artefacts caused by imaging voxels containing different tissues and therefore presenting a signal average of all tissues present, were created by averaging the voxel intensities of the centre slice and two adjacent slices. This also leads to a more realistic slice thickness. Gaussian noise was not added in the 2D scans due to its incompatibility with automatic template generation. The quantitative nature of this work requires consistency in

Table 3.1 Relevant anatomical and physiological parameters for the default 4 dimensional extended cardiac-torso (XCAT) male and virtual patients.

Patient	**LA Volume**	**LA Respiratory Motion**			**Heart Rate**	**Respiratory Rate**
	(ml)	AP (mm)	LR (mm)	SI (mm)	(bpm)	(cycles per min)
Default	65.7	12.0	1.0	20.0	60	12.0
1	73.1	14.0	1.2	27.0	65	14.4
2	88.6	10.1	2.7	16.7	66	15.2
3	104.8	1.0	4.9	15.6	75	13.1
4	92.1	8.5	2.1	25.5	59	13.9
5	104.0	6.5	5.2	9.6	68	11.5
6	79.5	8.5	2.6	12.0	54	15.5
7	102.2	7.2	1.2	14.8	42	10.8
8	77.3	2.7	4.0	11.8	64	13.0
9	69.0	6.8	2.7	23.1	69	16.5
10	103.5	7.4	3.5	23.5	64	12.0
11	119.8	5.8	2.5	8.4	48	13.2
12	55.2	7.1	3.3	16.9	50	11.6
13	89.7	2.9	3.9	9.3	56	13.0
14	122.6	14.7	4.2	15.5	54	10.5
15	49.4	1.8	2.5	17.2	79	14.6
16	94.6	6.4	4.5	26.7	78	13.6
17	103.5	8.8	3.9	11.9	64	12.5
18	82.7	0.7	2.1	22.9	48	12.7
19	90.9	4.7	2.6	4.6	55	13.8
20	71.0	11.1	3.3	19.2	60	15.6

Table 3.2 The 4 dimensional extended cardiac-torso (XCAT) virtual patient study. 2D and real-time scan parameters.

Parameter	**2D scan**	**2D-2D real-time scan**
Scan direction	Sagittal	Sagittal - Coronal
In-plane voxel size	1.3 mm	2 mm
Slice thickness	5.1 mm	6 mm
Field-of-view (FOV)	318.5 mm^2	320 mm^2
Cardiac cycle	10 discrete phases	-
Temporal resolution	-	200 ms
Noise	-	Gaussian

the template generation, a feature that user specific template delineations can-not produce.

Finally, Sec.3.2.2 was repeated for 2 mm^3 isotropic 2D scans to investigate the impact of the 2D scan's spatial resolution on the tracking accuracy. This results in a decrease of spatial resolution detail from 1.3 mm to 2 mm for the in-plane pixels of cardiac template images. However, this allows for algorithmic testing on template and real-time images that are identical in voxel size.

3.2.3 Virtual patient real-time scans

The real-time scans were initiated to replicate the 2D cine free breathing scans from the previous study [34], detailed in Sec.2.3.2. The scan parameters used in the real-time image simulation are shown in Tab.3.2. Generation of the real-time phantoms follows the methodology explained in Sec.3.1.2 but a number of alterations to improve MRI realism were added. First, a temporal resolution of 200 ms was used across all virtual patient's real-time frames to represent the lower limit of acquisition times from Ipsen [34].

In order to simulate partial volume artefacts [4] a 2 mm^3 isotropic voxelised phantom was generated with its sagittal and coronal real-time planes being the mean pixel intensity of the central LA slice and two adjacent slices. This also creates real-time planes with six millimetre slice thickness as desired. Furthermore, Gaussian noise is added in the real-time scans based on a signal-to-noise ratio (SNR) of greater than two [27]. An example of the original and the resultant slice after these modifications is shown in Fig.3.5. This process is conducted on each real-time sagittal and coronal plane. Finally, Sec.3.2.3 was repeated for 2 mm^3 isotropic voxel real-time scans. This was conducted to investigate the effects of a higher level of spatial resolution on the tracking accuracy but excluded partial volume artefacts.

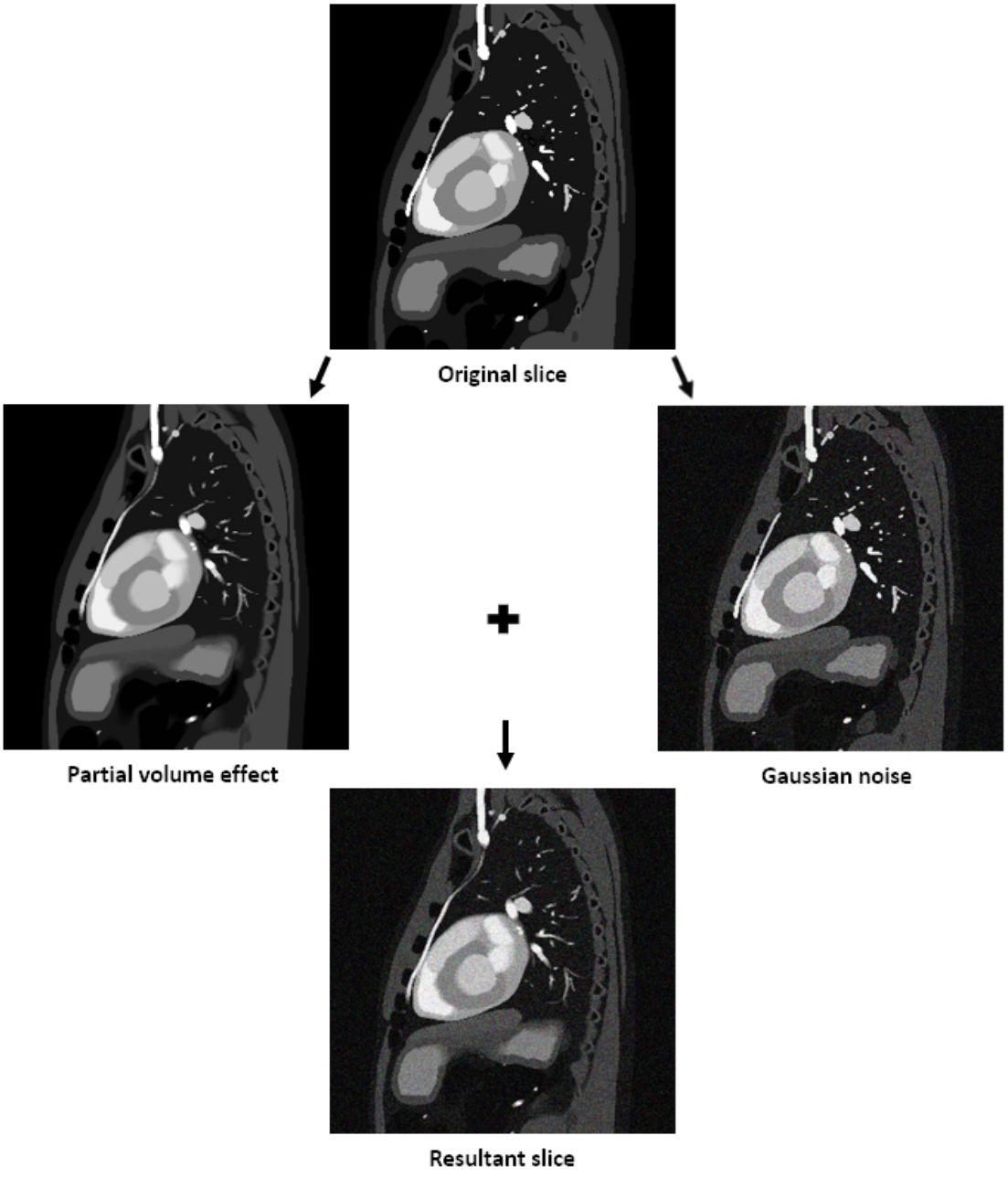

Fig. 3.5 The inclusion of partial volume artefacts and Gaussian noise. (Top) Original single slice. (Middle left) Central slices with averaged voxel intensities for the partial volume effect. (Middle right) The inclusion of Gaussian noise to the original single slice. (Bottom) Resultant image after both artefacts are included.

3.3 Developed tracking methodology and functions

Applying the original tracking method to the XCAT phantom data highlighted areas where improvements to the tracking algorithm could be made (see Sec.4.1). The presence of the XCAT ground-truth allowed algorithmic changes to be quantified. A variety of new functions were implemented and quantified with interfunctional compatibility considered in the design. These are described in the following paragraphs and were tested on the virtual patients described in the previous section (Sec.3.2).

An initialisation function scanning the entire template volume and real-time images to automatically align LA volumetric centres was added, on account of the results of Sec.4.1. This tracking method will be refered to as 'dual last position' (DLP) and differs from the original tracking method only through this initial alignment. The initialisation function is included in all the following algorithms. In an effort to further verify the work conducted by Ipsen [34] most functions were tested for a maximum-diastole/systole and end-diastole/systole dual template approach.

3.3.1 All template positions function

The 'all positions' template matching function seeks to reduce possible systematic errors that can arise using the original tracking where the last position's respective AP or LR matched location is used to determine current slice match location. As described in Sec.2.3.3 any misalignment at any stage of the tracking process is continued throughout the remaining matching procedure. By passing the entire 3D volume of the template, slice-by-slice, over each successive 2D real-time plane every current frame has a new attempt to discern a matching location. The matching forms a 3D similarity matrix as shown in Fig.3.6.

3.3.2 Bordered template function

The bordered template function adds a user definable number of blank voxels, void of LA volume but containing the adjacent anatomy to the outside of the 3D template volume. Preliminary experiments indicated that tracking accuracy was increased when matching with larger template volumes.

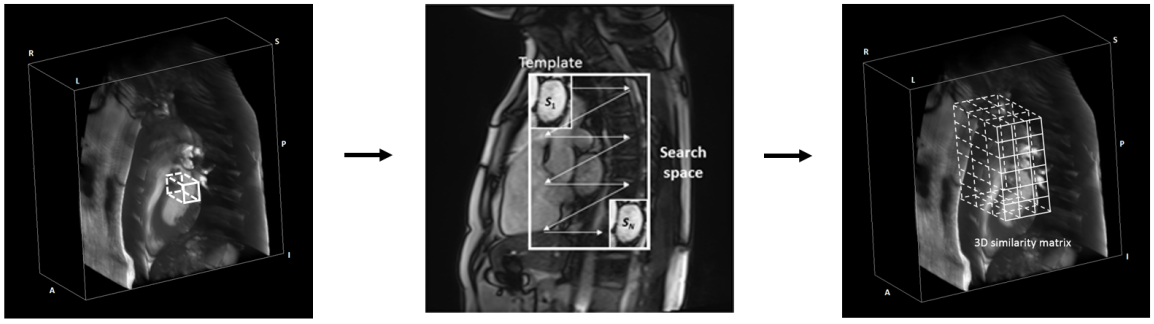

Fig. 3.6 'All positions' matching function. (Left) 3D scan containing template volume, white cuboid. (Middle) Each template slice is passed progressively over the real-time plane. (Right) A 3D similarity matrix is formed with highest similarity measure inferring volumetric real-time position.

3.3.3 Dynamic search function

Preliminary experiments with the tracking showed that matching location outliers were present when large search spaces were allowed for the template match. This is a result of image artefacts that in turn affect the similarity matrix by presenting a better pixel intensity match at an incorrect location. To increase tracking robustness a dynamic search function was implemented where successive matching locations can only be located within a user defined distance (based off observed and known LA motion trajectories) from the last matched location (Fig.3.7).

3.3.4 Isolated template function

The isolated template function seeks to remove the rectangular nature of the matching template by isolating only the 3D volume and matching it to the real-time planes. In this function the user delineation on each 2D breath-hold image is the entire target to be matched. There are no regions of anatomy adjacent to the LA in these templates unless included in the user delineation.

3.3.5 Tri-template function

The tri-template matching function expands upon the dual method by incorporating a third template to the matching method. In this case maximum-diastole, end-diastole and systole templates were used on account of their prominence throughout a single cardiac cycle. The template which is chosen for matching is based off electrocardiogram (ECG) signal binning. On account of literature values on the heart rhythm [57] the systole template is used for 30%

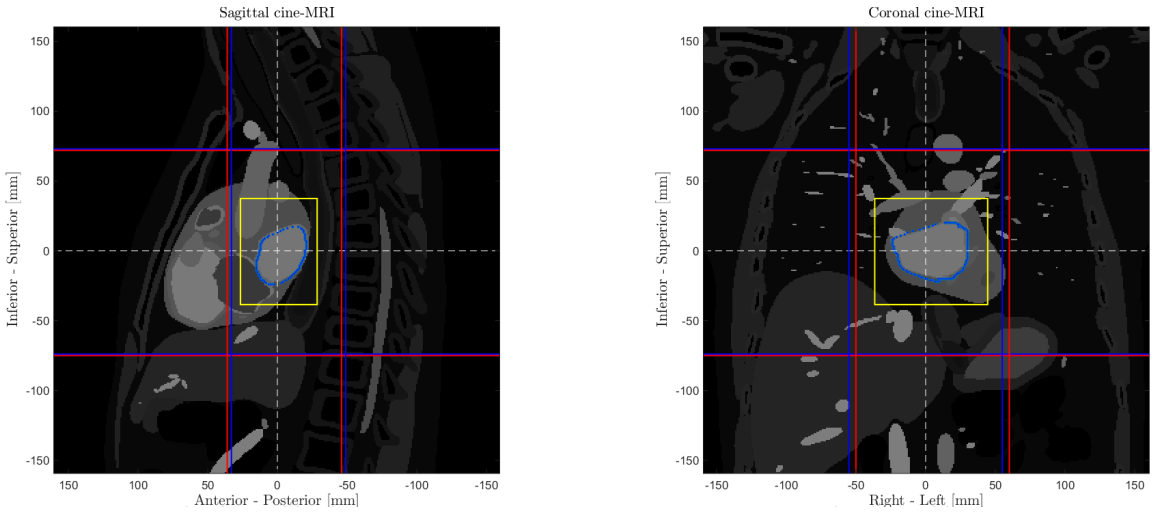

Fig. 3.7 Dynamic search function of successive sagittal (left) and coronal (right) planes of the XCAT model. The blue and red lines indicate the diastolic and systolic allowable search spaces respectively, while the blue delineation shows the tracked LA. The yellow polygons represent the dynamic search where the next matched location must be within these boundaries.

of the cardiac cycle, maximum-diastole for 10% while the remaining 60% of the heart cycle is matched with an end-diastole template. In cases where a current template is different from the last frame's matched template, the anatomical plane location that isn't updated (i.e. AP or LR) is inferred from the last template, in congruence with the original dual matching method. The tri-template method also incorporates the dynamic bordered (DB) function due to its superior tracking accuracy (Sec.4.2.1).

3.3.6 4D template function

Incorporating the ten cardiac phase templates into a '4D template' that constantly updates and fits within the current heart rate (last recorded R-R peak time interval) is the objective of this function. By shifting to a 4D scenario the cardiac contraction motion is more deliberately compensated for in the template, hence the motion primarily being tracked is the respiratory component. In comparison to the dual- and tri-template methods the 4D template updates all three anatomical plane locations every real-time plane. When the 'last position' method as opposed to the 'all positions' method is used with the 4D function it becomes a 2D matching strategy with the inclusion of time. These methods incorporate the DB function due to their superior tracking accuracy (Sec.4.2.1).

3.4 MRI data implementation

The final analysis that was conducted involved qualitatively assessing how the best performing virtual patient tracking function compared to that of the original tracking with real MRI data. The templates' LA centre trajectories for volunteer 5 over their real-time scan is displayed in the final results section of the previous study Ipsen [34]. Utilising the methodology developed in this work the absolute motion of this trajectory is discerned and compared to the absolute motion trajectories of the 'dual all positions dynamic bordered' (DAPDB) method. The DAPDB method is used as it gave the best tracking accuracy across the virtual patient standard resolution study and in the improved spatial resolution study (Sec.4.2.1). The search space used for the DAPDB method is significantly enlarged from the original tracking to further test tracking robustness.

4

RESULTS

Tracking accuracy demonstrated to be below the acceptable treatment margins described in Sec.2.3.1 would further promote magnetic resonance imaging (MRI) guided radiosurgery with an integrated MRI linear accelerator (MRI-Linac). The methodology behind a first quantitative measure for the cardiac tracking is introduced in the previous chapter and the tracking error results of these methods are presented here. The original tracking method is quantified in Sec.4.1. The tracking results of the virtual patient study for the multitude of tracking functions is explored in Sec.4.2. Lastly, a look at the newly developed function's performance on real-world data is the objective of Sec.4.3.

4.1 Ground-truth of original tracking

Assessment of the original tracking was conducted on the default male 4 dimensional extended cardiac-torso (XCAT) physiology phantoms with high spatial and temporal resolution. The mean 3D tracking error and the associated anatomical plane tracking errors of the original left atrium (LA) tracking method is shown in Tab.4.1. The tracking error is largest in the left right (LR) plane with 1.6 mm, followed by superior inferior (SI) of 0.8 mm and anterior posterior (AP) of 0.1 mm. In contrast to these errors, the phantom's respiratory motion magnitudes were highest in SI followed by AP and LR (also observed in Ipsen *et al.* [35]). For the default XCAT anatomies tested here a larger motion magnitude does not correlate to a larger tracking error. Comparison of the ground-truth motion and template matching motion is shown in Fig.4.1.

An analysis of these results revealed that template and real-time plane LA volumetric centres were not in perfect alignment. Even with the 1 mm isotropic voxel resolution it was difficult to achieve optimal visual positioning. To account for this the 'dual last position' (DLP)

Table 4.1 Tracking error associated with the original tracking method and 'dual last position' (DLP) method for the 4 dimensional extended cardiac-torso (XCAT) phantom.

	Tracking RMS error (mm)			
Default XCAT anatomy	SI	AP	LR	**3D**
Original tracking	0.8	0.1	1.6	**1.8**
DLP	0.6	0.1	0.2	**0.6**

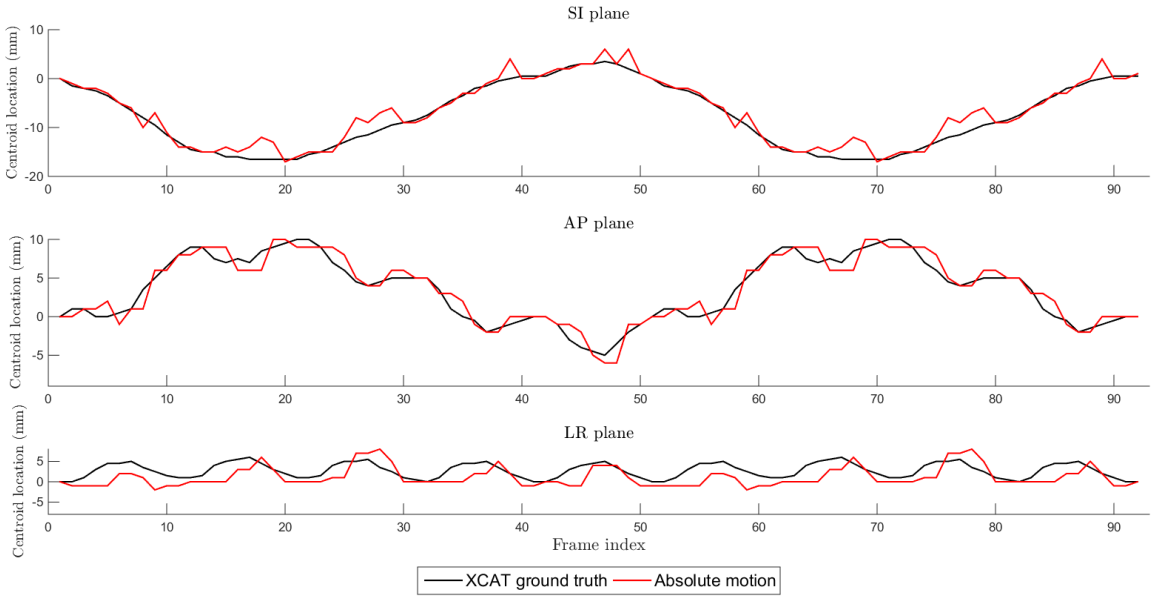

Fig. 4.1 Original tracking method's resultant trajectories on the 1 mm^3 default XCAT anatomical parameters.

method was tested for the same XCAT anatomies and the results are summarised in Tab.4.1. The mean 3D tracking error of 0.6 mm is one third that of the original method. This function was qualitatively assessed with the real MRI data and in initial experiments with the XCAT virtual study. Due to a positive result the function was permanently integrated into the base tracking algorithm used for the rest of this work.

4.2 XCAT virtual patient study

The main purpose of the virtual patient study is quantifying the developed cardiac tracking methods with simulations closely resembling the real-world procedure. To provide a measure of accuracy the template's centre position as determined by the tracking algorithm is compared with the ground-truth position of the centre of the LA's bounding box in the

real-time phantoms. A mean 3D tracking error is discerned in addition to the three anatomical plane constituent errors (SI,AP,LR).

A variety of new tracking functions (Sec.3.3) were implemented and assessed using this technique. In addition to the quantification, the presence of known and quantifiable physiological parameters of the virtual patients was analysed regarding information on how tracking could be optimised on a patient specific basis. The full results for all tracking functions on the virtual patients is detailed in the Appendix (Sec.A).

The following results section is broken into the accuracy assessment of the modified tracking methods, and the effect of an increased spatial resolution in the template and real-time images on tracking accuracy.

4.2.1 Tracking developments

All of the developed functions have integrated compatibility with one another. The original 'last position' template matching approach is compared against the new 'all positions' method for most of the developed functions. In this way it is easier to discern optimum combinations for specific patients.

The tracking error was first calculated for the DLP matching strategy. When matching with an end-diastole/systole template combination the mean 3D tracking error was 7.9 ± 3.9 mm compared to a 3.6 ± 2.1 mm tracking error with maximum-diastole/systole template (Tab.4.2). Matching with an end-diastole/systole approach proved more accurate than utilising a maximum-diastole template for the 'dual all positions' (DAP) method with 4.6 ± 2.8 mm and 5.4 ± 3.6 mm respectively (see Tab.4.2).

The bordered template function was quantified for the best case DLP approach (maximum-diastole/systole) and both of the DAP template approaches (maximum-diastole/systole and end-diastole/systole). The results are summarised in Tab.4.2. All tracking errors are improved with the inclusion of the bordered function. The maximum-diastole/systole (3.5 ± 2.7 mm) dual combination outperforms the end-diastole/systole (4.0 ± 1.7 mm) for the DAPB method however both are less accurate than the DLPB approach (3.2 ± 1.7 mm).

Application of the dynamic bordered (DB) search function onto the best performing

Table 4.2 Mean 3D tracking and anatomical plane error and their standard deviations for the 20 virtual patients with the various tracking function combinations. 'Dual last position' (DLP). 'Dual all positions' (DAP). 'Dual last position bordered' (DLPB). 'Dual all positions bordered' (DAPB). 'Dual last position dynamic bordered' (DAPDB). 'Dual all positions dynamic bordered' (DAPDB). 'Tri-last position' (TLP). 'Tri-all positions' (TAP).

Approach	**Mean tracking error (mm)**			
	SI	AP	LR	**3D ± std**
DLP *(max-dia/sys)*	1.9 ± 1.3	1.6 ± 1.2	2.2 ± 1.8	**3.6 ± 2.1**
DLP *(end-dia/sys)*	3.0 ± 2.2	3.2 ± 1.8	6.2 ± 3.5	**7.9 ± 3.9**
DAP *(max-dia/sys)*	1.0 ± 0.5	1.2 ± 0.8	5.0 ± 3.8	**5.4 ± 3.6**
DAP *(end-dia/sys)*	2.1 ± 1.4	1.0 ± 1.0	3.3 ± 3.1	**4.6 ± 2.8**
DLPB *(max-dia/sys)*	1.3 ± 0.9	1.4 ± 0.9	2.2 ± 1.8	**3.2 ± 1.7**
DAPB *(max-dia/sys)*	0.7 ± 0.7	1.5 ± 1.1	2.6 ± 2.9	**3.5 ± 2.7**
DAPB *(end-dia/sys)*	1.1 ± 0.8	2.1 ± 1.1	3.0 ± 1.8	**4.0 ± 1.7**
DLPDB *(max-dia/sys)*	1.3 ± 1.0	1.4 ± 0.9	2.0 ± 1.8	**3.1 ± 1.7**
DAPDB *(max-dia/sys)*	0.9 ± 0.5	1.6 ± 0.8	1.6 ± 2.0	**2.9 ± 1.6**
TLP	1.2 ± 0.9	1.8 ± 1.0	2.3 ± 1.4	**3.5 ± 1.1**
TAP	1.4 ± 1.2	2.1 ± 1.0	2.5 ± 1.8	**4.0 ± 1.6**
2D + time	1.4 ± 1.5	1.8 ± 1.2	3.4 ± 2.0	**4.5 ± 2.1**
4D	1.0 ± 0.9	1.8 ± 1.1	2.5 ± 1.9	**3.4 ± 2.0**

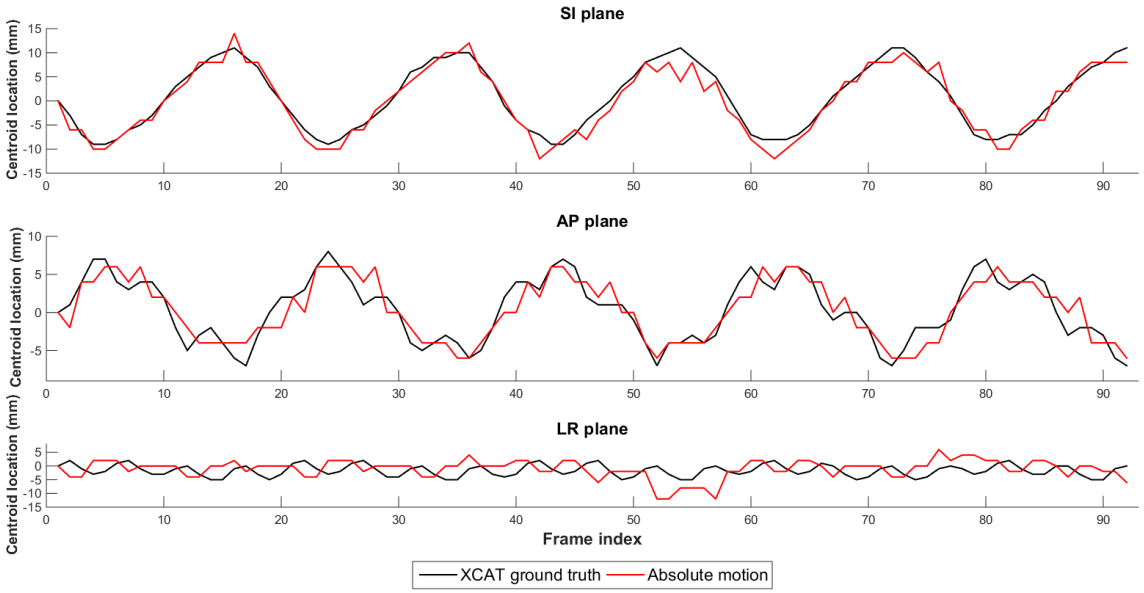

Fig. 4.2 Resultant trajectories using the DAPDB function for virtual patient 20

approaches gives the most accurate result that is seen across the virtual patient study at standard spatial resolutions. The mean 3D tracking error as shown in Tab.4.2 is 3.1 ± 1.7 mm and 2.9 ± 1.6 mm for the 'dual last position' and 'dual all positions' dynamic bordered (DLPDB, DAPDB) methods, respectively. The best performing virtual patient (patient 20) had submillimetre 3D tracking error when the DAPDB method was applied. Patient 20's trajectory comparison is shown in Fig.4.2. The ground-truth trajectory is smooth in the SI position due to its positional change uniformity throughout the cardiac cycle and is followed most of the time by the template matched SI trajectory. The high frequency components in the AP ground-truth direction are due to the periodic cardiac contraction and are mostly followed by the template matching. The low frequency components are due to the respiratory cycle. Both LR trajectories contain both motion components but it is difficult to discern a difference due to the small magnitudes and two notable matched outliers.

The isolated template function produced the highest values for tracking error across the entire virtual patient study and was ceased after five patients due to its poor performance. The results are not displayed in Tab.4.2 but can be found in the Appendix (Sec.A).

The tri- and 4D template matching methods exhibited tracking errors comparable with the errors from earlier in Sec.4.2.1. These errors are outlined in Tab.4.2. The method with the lowest mean tracking error is the 4D template matching approach with 3.4 ± 2.0 mm.

Almost all methods showed highest tracking error in the LR plane followed by AP and SI. The only exceptions were the DLP maximum-diastole/systole and DAP end-diastole/systole functions where LR is still the anatomical plane with the highest error but is followed by the SI plane and then AP.

The effect of varying physiological parameters on the tracking accuracy was analysed using statistical correlation [52] and significance. The results are visualised in Fig.4.3. These results focus on the DAPDB matching method which demonstrated the best overall accuracy while still being representative of the other investigated tracking functions. As the number of cardiac and respiratory cycles per minute increases there is a general trend towards a higher tracking error. A smaller LA volume is associated with an increase in tracking error. The LA respiratory motion magnitude affects the tracking accuracy in an inconsistent manner. A decrease in AP motion is associated with a higher tracking error while a decrease in LR motion is associated with a lower tracking error. The extent of SI respiratory motion of the LA shows no correlation with the tracking accuracy. A patient's heart rate is the only statistically significant (p-value < 0.05) anatomical parameter influencing tracking accuracy, its linear relationship is shown in Fig.4.3.

Additionally, Fig.4.4 demonstrates that different tracking approaches do not have identical tracking accuracy for the same patient. Patients 6 and 12 show very effective tracking for one or two methods while exhibiting more average tracking accuracy for the remaining methods. Patients 3, 15 and 16 exhibit consistently higher tracking errors across all tracking methods. The optimal tracking method is therefore patient-specific as is the lowest achievable tracking error.

4.2.2 Spatial resolution manipulation

In order to assess how the tracking accuracy is affected by increasing spatial resolution the matching errors of the 4D tracking and DAPDB functions were quantified. The 4D method was chosen due to its volumetric information that considers more of the contractile motion components while the DAPDB function was assessed based on the achieved best tracking accuracy across the standard resolution virtual patient study.

The 2D scans used for template generation as well as the 2D-2D real-time scans were subject to an increase in spatial resolution detail for slice thickness. The 2D template scan's detail was increased from 5.1 mm to 2 mm and the 2D-2D real-time scan's detail was increased

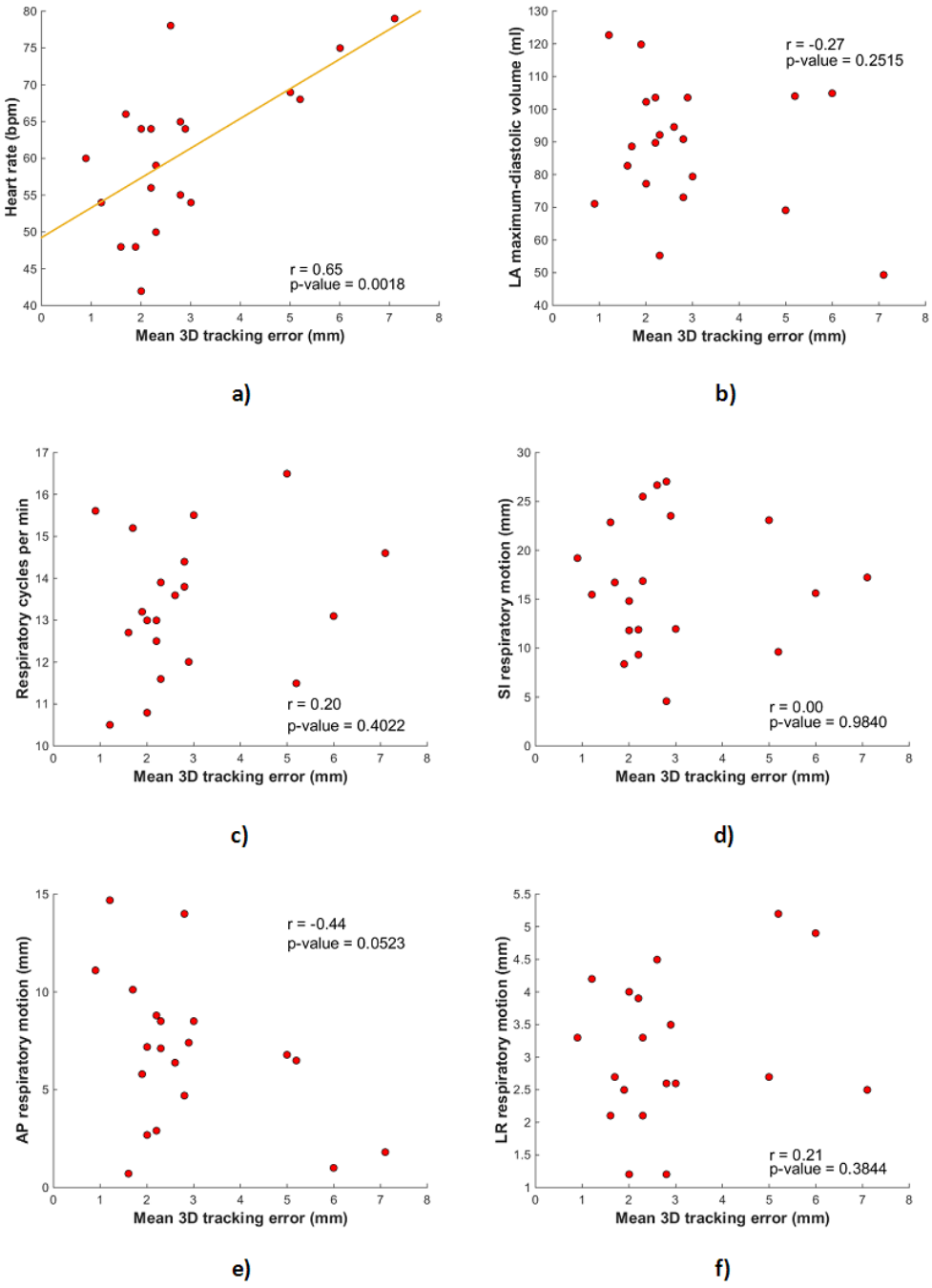

Fig. 4.3 Mean tracking 3D error against physiological parameters of the 20 patient virtual study using the 'dual all positions dynamic bordered' (DAPDB) method with corresponding Pearson correlation and p-value. Mean 3D tracking error against **(a)** Heart bpm. **(b)** LA maximum-diastole volume. **(c)** Respiratory cycles per min. **(d)** SI respiratory motion. **(e)** AP respiratory motion. **(f)** LR respiratory motion.

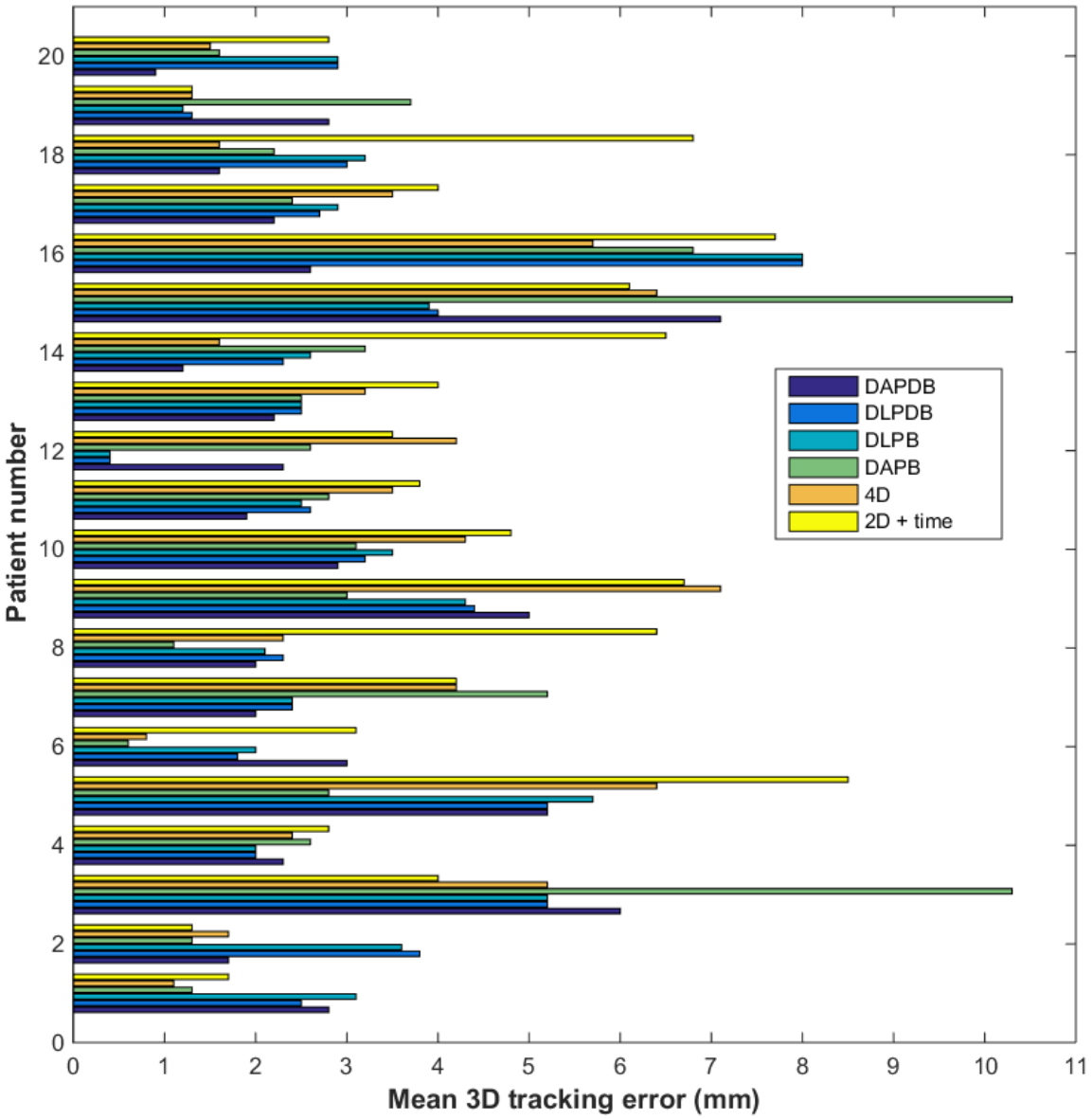

Fig. 4.4 Mean 3D tracking errors for different matching approaches across the 20 patient study. 'Dual all positions dynamic bordered' **(DAPDB)**. 'Dual last position dynamic bordered' **(DLPDB)**. 'Dual last position' **(DLPB)**. 'Dual all positions' **(DAPB)**.

Table 4.3 Mean 3D tracking and anatomical plane error and their standard deviations for the 20 virtual patients with the 4D template and 'dual all positions dynamic bordered' (DAPDB) functions. Cardiac template and real-time image spatial resolution manipulation.

	Mean tracking error (mm)			
4D	SI	AP	LR	**3D ± std**
2 mm^3 2D template scans	0.7 ± 0.6	1.4 ± 0.8	2.5 ± 1.9	**3.2 ± 1.7**
2 mm^3 2D template and RT scans	0.9 ± 0.7	1.2 ± 0.8	3.0 ± 2.0	**3.6 ± 2.0**
DAPDB				
2 mm^3 2D template scans	0.8 ± 0.7	1.5 ± 0.6	1.8 ± 1.9	**2.7 ± 1.7**
2 mm^3 2D template and RT scans	0.8 ± 0.7	1.5 ± 0.8	1.9 ± 1.7	**2.8 ± 1.5**

from 6 mm to 2 mm. The results of increasing the spatial resolution detail for the template scans only, and the results for the increase in both template and real-time scans is shown in Tab.4.3. When utilising the 4D matching approach under higher resolved template images there is a slight increase in tracking accuracy to 3.2 ± 1.7 mm from 3.4 ± 2.0 mm. Increasing both scan resolutions results in a slight decrease in tracking accuracy to 3.6 ± 2.0 mm. A slight increase in the tracking accuracy is seen when using the DAPDB function for both variations of the spatial resolution manipulation and the highest tracking accuracy in this work of 2.7 ± 1.7 mm was achieved (increased resolution of the 2D template scans only).

4.3 MRI patient traces

The trajectories of the original tracking method compared with the best performing method found in this work are shown in Fig.4.5 for scanned volunteer five. Due to the lack of a real-time volumetric ground-truth it not possible to provide a quantitative accuracy measure of the new method. The DAPDB method tracks the deep inhale observed at the beginning of the real-time scan (see SI plane). Qualitatively, motion spikes in the AP and LR plane have been reduced with the DAPDB method. This is likely due to the inclusion of the dynamic search function. The discrete nature of the dual template matching results in corresponding matching "blocks" for both methods. LR motion appears to be tracked more accurately with the DAPDB method as the magnitude falls mostly within expected and observed LA motion values. Enlarging the search space for the DAPDB method does not appear to have any immediate effect on the tracking trajectories. Based on the results of the virtual patient

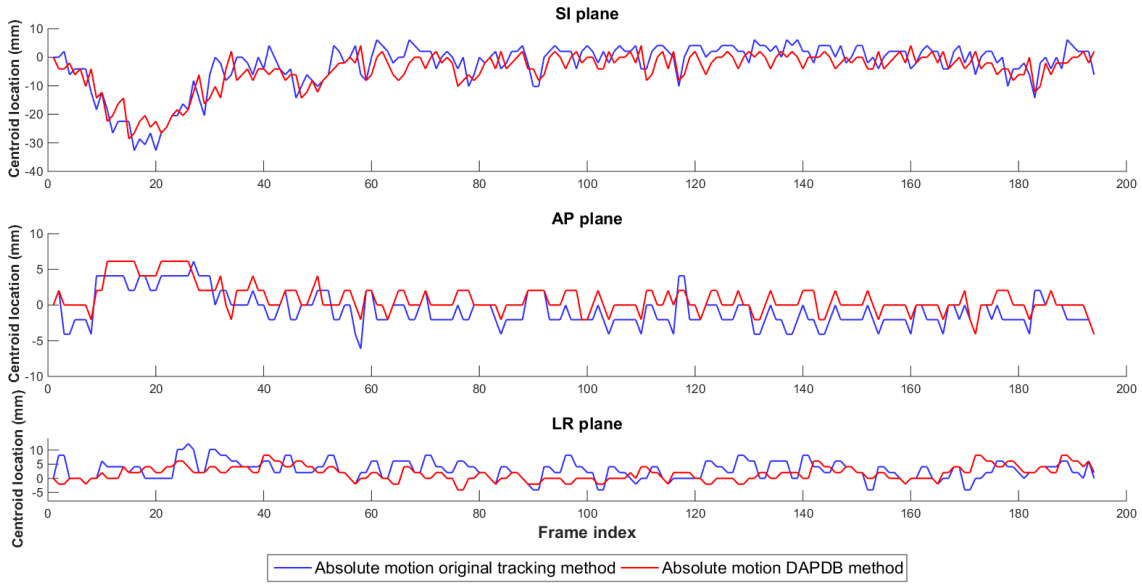

Fig. 4.5 Comparison of absolute motion for the original and DAPDB methods on volunteer five.

XCAT study it is expected that the mean 3D error of the DAPDB method is approximately 3 mm.

5

DISCUSSION

The work investigated in this thesis provides development, analysis and quantification of cardiac tracking towards a magnetic resonance imaging (MRI) guided radiosurgery treatment of atrial fibrillation (AF) with MRI linear accelerator (MRI-Linac) technology. The lack of 4D MRI anatomical data restricts an ideal ground-truth from being ascertained. Complex respiratory and contractile motion of the LA further complicates quantification measures. The 4 dimensional extended cardiac-torso (XCAT) phantom is utilised in this investigation due to its realistic anthropomorphic anatomy and physiology and quantitative capabilities. The XCAT phantom allows comparison to measured trajectories to a ground-truth in order to quantify the accuracy of the tracking and to further elucidate assumptions arising from Ipsen [34]. Thorough examination of the cardiac tracking within a digital environment and a concise extension to MRI data is conducted in this chapter.

The importance of an available ground-truth with the XCAT phantom cannot be overstated. Based on real imaging data the XCAT's subdivision and non-uniform rational basis spline (NURBS) surfaces realistically model anthropomorphic physiology. Its use in developing novel imaging simulations and image interpretation strategies has been described in Sec.2.4. In this thesis the XCAT's known motion trajectories have allowed improved tracking methods to be developed, in addition to analysing how patient specific physiologies interact with different tracking algorithms. In order to achieve the complex quantification with the XCAT phantom the original tracking was replicated on a spatially and temporally high resolved scenario before being applied to a more realistic XCAT simulation incorporating frequent artefacts. In a final experiment, the spatial resolution detail of the 2D template and real-time scans were increased to assess the effect on tracking accuracy.

The virtual patient study with identically modelled MRI scan parameters provides the most

significant results of this thesis. Employing a tracking method with the same basic methodology as the original tracking on a realistically simulated virtual patient cohort resulted in a mean 3D tracking error of 3.2 ± 1.7 mm. The best tracking function for the virtual patient study, a dual template (maximum-diastole/systole) volume that includes a small region of adjacent anatomy that confines the next location match, reduced the matching error to 2.9 ± 1.6 mm.

5.1 High spatially and temporally resolved simulation

The analysis of the original tracking served as a reverse engineering project. Before the availability of the XCAT ground-truth many qualitative observations and assumptions guided tracking design. A perfect digital scenario provided insight into the efficacy of such designs. Utilising the original tracking with 1 mm isotropic voxels and 100 ms acquisition times resulted in a mean 3D tracking error of 1.8 mm. An automatic function to align template and real-time plane volumetric left atrium (LA) centres was written. Previously, the alignment was conducted visually and was prone to errors because of its subjective nature. It is expected that this difficulty would be more pronounced in the proposed MRI workflow. When implementing this function the mean 3D tracking error was 0.6 mm, a large improvement that exhibited subvoxel accuracy. This component of the work provided proof-of-concept for the tracking procedure with a quantitative measure. However, these results cannot be inferred to a real-world scenario due to their perfect and therefore unrealistic nature.

The most notable limitation of this study is the spatial and temporal resolutions. A 1 mm isotropic voxel size and assumed 100 ms acquisition times are beyond the capabilities of current MRI technology for the scan types required in this work. Image resolution for similar 2D breath-hold scans can be less than 2 mm^3 [12] but current steady-state free precession (SSFP) imaging such as the Siemens true fast imaging with steady state precession (TrueFISP) typically use slice thicknesses of 5 - 8 mm for real-time environments [45, 46].

It remains unclear how pragmatic an automatic function to align template and real-time plane volumetric LA centres would perform on MRI data. The function itself is relatively simple however involves an entire template volume match to initialise real-time planes. Similar to the general tracking methodology, errors in the matched alignment due to image artefacts may be present. Having more possible matching locations implies more possibilities for an incorrect match. However, this centralisation function demonstrates that when there is

perfect alignment of LA centres the tracking performs exceptionally well. These are in addition to the general limitations of the XCAT phantom which are described in Sec.5.2.3.

5.2 Virtual patient study

A 20 patient virtual study simulated to more accurately model the real-world MRI workflow extended the quantification of Sec.4.1. The study provides greater understanding of how tracking methods may perform over a general population and how patient's anatomical parameters influence tracking functionality. Anatomical XCAT pixel values in this work are assigned based on observed values in the MRI scans. Cai *et al.* [14] utilised this method when replicating TrueFISP MRI images of the abdomen and it is also used in realistic cardiac MR simulations reported by Tobon-Gomez *et al.* [68]. On account of this feature the work performed in this thesis can easily be extended to future tracking developments which could incorporate different MRI sequences. Therefore cementing the XCAT virtual study as a vital tool in future algorithmic quantification. Furthermore, the rather artificial appearance of the initial tracking images were noticeably improved with the inclusion of partial volume artefacts and image noise in the virtual patient study. However, despite these advantages the shape, dynamics and image presentation of the LA are simplified. Many originate from general XCAT limitations which are discussed in Sec.5.2.3 but inclusion of respiratory motion artefacts, additional cardiac structures [68] and larger image contrast differences would further improve the virtual patient simulations.

5.2.1 Tracking accuracy

Ground-truth motion was compared to the template matching trajectories for fifteen different tracking function combinations with scan parameters representing the original MRI scans. For the four volunteers scanned in Ipsen [34] the best 2D mean tracking error was 3.0 mm. The method was extended to the 3D scenario and tracking error was inferred to be of similar accuracy. For the XCAT virtual patient simulation presented here the function that most closely simulates the foundation tracking developed in Ipsen [34], although included the centralisation function and full LA border, resulted in a mean 3D tracking accuracy of 3.2 ± 1.7 mm. This result is strongly congruent with the inferred and assumed 3D tracking error from Ipsen [34]. Further to observations from the previous work, when utilsing the dual template approach a maximum-diastole/systole combination consistently outperformed an end-diastole/systole combination. It is thought that the larger size of the maximum-diastole volume led to more robust localisation but the exact reasons remain unclear.

The remaining combinations of tracking functions focussed on algorithm development to increase real-time positioning accuracy. The best performing function 'dual all positions dynamic bordered' (DAPDB) error achieved a mean 3D tracking error of 2.9 ± 1.6 mm (0.9 ± 0.5 mm in the superior inferior (SI) plane, 1.6 ± 0.8 mm anterior posterior (AP), 1.6 ± 2.0 mm left right (LR)). The magnitude of tracking improvement from above is small. Results from Sec.4.2.2 imply that increased spatial resolution of the scans can improve tracking accuracy. In the virtual patient study, the highest mean 3D accuracy was 2.7 ± 1.7 mm. Again, the magnitude of improvement is small. These two results suggest that small optimisations of the tracking algorithm and increases in spatial resolution do not improve tracking accuracy as much as intuitively perceived. Changes to the tracking procedure workflow that could significantly increase tracking accuracy are explored in Sec.5.3. The 4D tracking method exhibits comparable tracking errors to the DAPDB function for both standard and increased spatial resolutions. This method increases the total number of discrete phase templates to ten. This more accurately compensates for cardiac contractile motion although it is yet to be determined how absolute motion of a specific target location could be interpreted by the linear accelerator (linac). However, incorporating more cardiac contractile information does not appear to hinder tracking accuracy.

It remains to be quantitatively proven if an 'all positions' search function would perform better than the original 'last position' function on MRI data. The difference in tracking errors for the two functions were small across the virtual patient study. The volumetric 'all positions' search is advantageous in that every new target localisation is conducted on the entire volume, removing any residual errors. However, the introduction of more matching locations on the often artefact heavy images could introduce more opportunities for an incorrectly matched location. If artefacts are shown to cause numerous mismatches on MRI data it may be beneficial to utilise a 'last position' matching method requiring further investigation. Nevertheless, the virtual simulations show a trend towards an 'all positions' approach at standard and higher spatial resolutions and qualitative improvements are seen for volunteer seven (see Sec.4.3).

It should be noted that throughout the tracking process across the XCAT work there are target matched locations which are outside expected motion ranges. This is due to the algorithm defining a better similarity match at an incorrect location due to influence on pixel values from image artefacts. These mismatches are also seen on MRI data. Although the mean tracking error is below acceptable margins these matched locations are not and must

be factored into the eventual motion compensation strategy. During treatment delivery these "jumps" could be detected as outliers and cause a beam-hold until matching is re-stabilised. A motion compensation strategy that represents a gated-tracked fusion may be the resultant approach for optimum treatment.

5.2.2 Physiological parameter influence

Patient 15 with coincidentally the fastest heart beat and smallest LA volume generally produced the worst tracking results across the virtual patient study. Heart rate is the most influential factor affecting tracking accuracy demonstrating a statistically significant Pearson's correlation of 0.65. To further support this, the virtual patients with faster heart rates are shown to exhibit poor tracking accuracy in comparison to the remaining patients. Acquisition times of 200 ms indicate that for fast beating hearts, a significant amount of information is lost between real-time planes. Computation times are not considered in this work due to continual improvements in computer processing and the possibility for this tracking to be run on graphics processing units. However, computation times and through-plane locations only being updated every second plane would further accentuate this effect. Medication to slow heart rate [32] before the radiosurgical procedure is one option which could increase tracking accuracy. The following three paragraphs are intended to give a qualitative first look at how the remaining patient parameters could influence tracking accuracy for future AF patients.

A larger LA volume is associated with a more robust tracking accuracy for virtual patients that exhibit more average values for the remaining parameters. The larger geometry is easier for the tracking to identify and hence localise due to a larger number of target pixels being matched in the real-time images. Interestingly, a larger LA volume while easier to track in this work has been associated with less successful outcomes of catheter ablation surgery for AF [1, 31]. It is yet to be discerned how this relationship translates to a radiosurgery treatment.

Respiratory cycle length does not appear to impact tracking accuracy, patients with short and long cycles show comparable results. However, respiratory parameters modelled with the XCAT phantom represent uniform amplitude and periodicity. In treatment scenarios a patient's respiratory motion could incorporate far more irregular patterns [13]. Deep breathing followed by shallow or static periods or sudden reverses are patterns which are not tested here.

The extent of respiratory motion in the three anatomical directions and their effect on tracking accuracy appears to be a complex problem. For the best performing tracking function at standard spatial resolution the SI magnitude has little to no effect on the tracking error while lower LR motion is associated with better tracking results and lower AP motion with worse. It is important to note that these trends are universal across all tested tracking functions and all tested virtual patients. One possible explanation is that the AP position is based off the last LR location which is consistently giving the largest tracking error due to the irregular LA shape and decreased resolution detail in the template's LR direction. However, the increased spatial resolution scans did not reverse the trend. Alternatively, the multitude of interacting anatomical parameters may obscure an independent comparison with tracking error. It remains unclear why AP-shifts follow this relationship therefore further investigation is warranted.

5.2.3 Virtual study and XCAT limitations

The uniform temporal resolution of 200 ms for the real-time planes is a limiting factor in this study for two main reasons. Firstly, a constant acquisition time is not seen in the real-time scenario for technical reasons and ranges from 200 - 252 ms [34]. Secondly, the XCAT produces a phantom at 200 ms intervals with instant acquisition. This is not coherent with a MRI acquisition time where cardiac and diaphragmatic motion would be present. The XCAT study assumes constant respiratory cycle lengths and heart rates and does not factor any intra-treatment variation. Additionally, deformation to the heart from respiratory influences [49] is not fully considered as the templates are derived from phantoms at full exhale. Deformation to the templates from any other phase of the respiratory cycle is not considered. Further to this, the XCAT templates are automatically delineated on the same 'breath-hold' phantom and hence achieve perfect alignment. In the real-world procedure the breath-hold nature of the template scans can lead to geometric misalignment for the templates. The XCAT work therefore represents an ideal scenario. The small patient cohort of only twenty healthy models also restricts extended generalisations. However, the virtual study does provide quantification information which was previously unavailable. Virtual studies of LA motion trajectories characteristic of AF have not been investigated.

Despite the realistic simulations the XCAT phantom's most obvious limitation is its digital nature. Tissue appearance, tissue motion and imaging modality replication are areas where the XCAT realism can be improved. Each anatomical structure is modelled in a homogeneous manner, organs and their sub-structures are of the same pixel value. As a result, image artefacts due to tissue heterogeneity are not simulated realistically. Partial

volume and noise artefacts were added here manually. Numerical single organ phantoms exist that more accurately model tissue heterogeneity [82] but cannot provide the patient variability or multiple organ interactions that were required in this work. The developers of the XCAT phantom are investigating a finite-element (FE) approach to further improve organ motion and interaction. The left ventricle has already been modelled in this manner [74]. FE design could allow physiological parameters (cardiac remodelling, blood flow, air flow, volume change, and lung pressure volume curve) to control and manipulate motion [62]. Future iterations of the XCAT phantom will minimise these limitations and further promote its use in imaging simulation strategies.

5.3 Towards cardiac radiosurgery

Tracking the heart with MRI in a real-time environment is a challenging task. The elaborate interaction of respiratory and contractile motion is the basis for this complexity. The best performing XCAT tracking function was tested on MRI data and was qualitatively assessed to show improvements. Based on the 2D tracking results of Ipsen [34] and the virtual study work in this thesis it is assumed the current mean 3D tracking error is of the order 3 - 4 mm. The following section explores this implication in the context of the current MRI target localisation method before looking at potential project developments.

5.3.1 Implications for MRI real-time tracking

The tracking errors inferred from the work to date are larger than those seen in similar 3D MRI localisation techniques. Brix *et al.* [12] infer 3D motion of the liver from single 2D image series through comparison to a 3D prescan volume. Submillimetre 3D tracking accuracy was demonstrated on their rigid ground-truth structure. Bjerre *et al.* [6] demonstrated 3D tracking accuracy slightly over 1 mm when utilising a 3D-2D approach similar to this work in an effort to track the kidney. The difference in accuracy is likely caused by the much more complex cardiac motion. Through-plane motion and deformation are more pronounced and harder to accommodate for cardiac structures. Orthogonal MRI has been investigated for healthy vascular [69] and tumour motion [64] for lung applications. These studies further demonstrate the feasibility of orthogonal MRI tracking. The results of the cardiac tracking to date indicate that lung tumours influenced by myocardial motion could be tracked using the electrocardiogram (ECG) surrogate approach. In fact, any area of the body affected by pulsatile motion could be compensated for in this way.

As discussed in Ipsen [34] utilising the ECG for template selection could translate to different multi-leaf collimator (MLC) configurations. The ECG selected template could have predefined MLC leaf arrangements which change with the discretised heart cycle. A dynamic MLC system investigating this possibility is detailed in Ge *et al.* [24]. The 4D tracking method introduced in this work could be even more mechanically demanding than a dual phase approach and should be the subject of future investigation. Deformation of the heart due to respiratory motion [49] could further add to the template library. The addition of a respiratory aid such as audiovisual biofeedback [41] would potentially be beneficial if respiratory motion was to be compensated.

Concerns remain whether the ECG surrogate tracking could successfully be used for a patient exhibiting AF at the time of treatment. At this stage only healthy volunteers with detectable R waves have been scanned. These are discernible even with distorted ECG signals from magnetic field interference. The resultant ECG signals of such a scenario for patients presenting with AF, or during an intermission period, have not been investigated. However, a patient in an AF period may exhibit lower contractile motion and could therefore be compensated for using the current method requiring only one template. Furthermore, it is not clear if compensating for cardiac contractile motion is of clinical significance. Teo *et al.* [67] demonstrated that 2 mm margins can account for up to 1 cm of cardiac contractile motion. This is a value much larger than observed target motions [42] which would likely be seen in this radiosurgery application. In this case, only respiratory real-time compensation would be required which could potentially also reduce the matching to a single template and remove the ECG surrogate.

It should be noted that the volunteer scans and consequential XCAT models were based upon the 3T MRI scanner. The final MRI-Linac field strength of 1T will present a lower signal-to-noise ratio (SNR) and contrast. Ipsen [34] details this as a possible advantage due to artefact reduction. Tracking algorithm's performance on lower field strength scans will require further investigation.

5.3.2 Further developments

From the results of the XCAT parameter evaluation it is clear that rapid heart beats cause discrepancies in the tracking accuracy. Medication was proposed as a method to slow the heart rate but the image acquisition method could also be changed. Advances in real-time MRI could allow for much shorter acquisition times [73] than used in the proposed MRI workflow. Slice thickness is increased in these images but may not adversely affect tracking

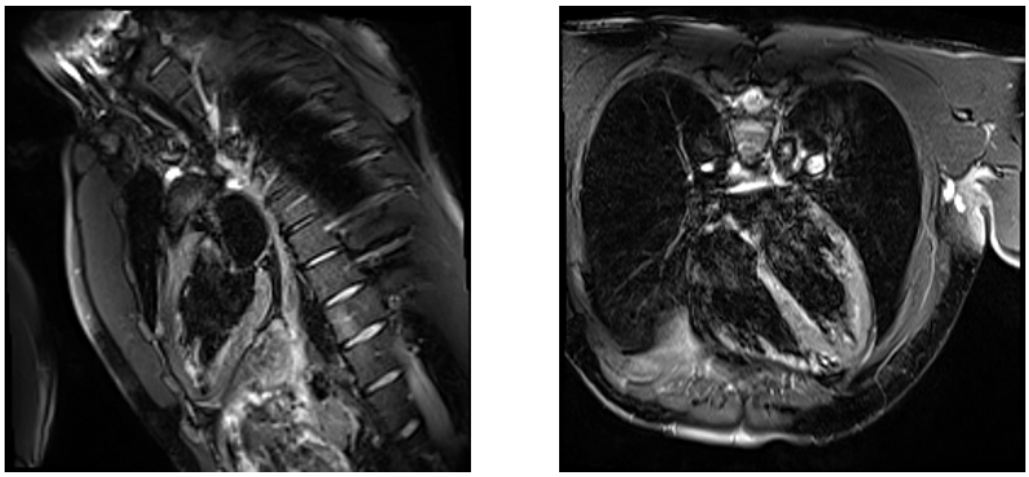

Fig. 5.1 Black-blood orthogonal MRI of volunteer seven. (Left) Two chamber view. (Right) Four chamber view

accuracy. This is supported by the tracking errors of the virtual patient experiments with varied spatial resolution. Images used for template generation appear to require higher levels of spatial resolution in comparison to the real-time images. Black-blood MRI is another possible method of improvement and a preliminary scan of volunteer seven is shown in Fig.5.1. Single-shot cardiac black-blood techniques can have imaging times slightly shorter at 180 ms [75] and distinct contrast between LA blood pool and the myocardial wall could aid in correct target location similarity matches. A new imaging protocol using black-blood techniques would not require significant alteration of the current tracking methodology.

At present, templates are manually delineated on the 2D breath-hold scans. The high contrast often seen in these images makes the LA boundaries difficult to discern. The subjective nature of the process implies errors due to inter-user variability. Intra-user variability error could also occur if templates were generated at different times. Automatic segmentation is a feasible strategy to remove this potential error and improve consistency. An atlas-based segmentation method for the LA has already been established [21] and initial experiments with computer learning showed promise. Training the algorithm with a support vector machine (SVM) to distinguish areas of LA from adjacent anatomy was investigated and is shown in Fig.5.2. For slices containing significant LA volume the automatic delineation performed well. Black-blood MRI and automatic segmentation hold high potential yet the goal of this thesis was to provide the missing quantification of cardiac tracking. Future developments could pursue a permanent integration of these methods into the tracking workflow.

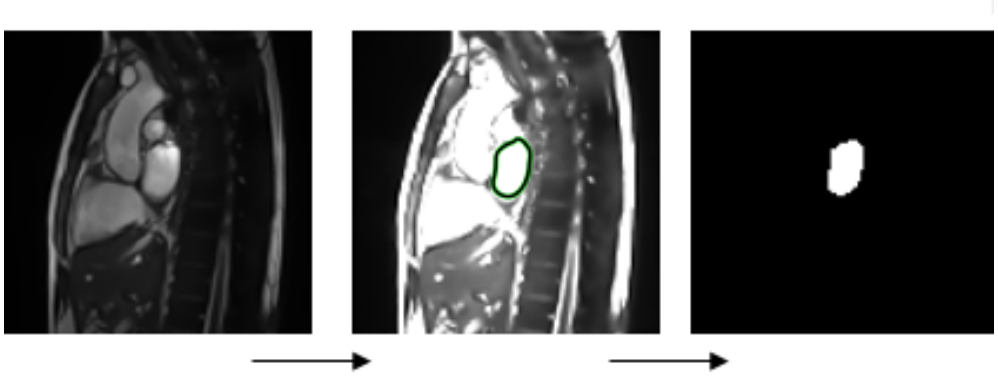

Fig. 5.2 Automatic delineation of patient seven's LA using SVM based computer learning. (Left) Input image. (Middle) Input image subjected to SVM classifier. (Right) Automatically segmented LA.

Moving away from template matching could also increase tracking accuracy. A multitude of approaches which could be adapted for this purpose have been investigated, for example active appearance models or FE deformable models for tracking the heart in cardiac MRI [58]. Additionally, the use of dynamic elastic models with MRI [60] and thin-plate spline tracking of the heart surface [59] have been used for cardiac tracking.

However, the results of this thesis and the work by Ipsen [34] show that acceptable tracking accuracy can be achieved by utilising a real-time motion compensation strategy based on simple template matching. Treatment plans with margin sizes less that 5 mm were within acceptable limits for the single patient study by Ipsen *et al* [35]. This indicates that a non-invasive radiosurgical treatment for AF could potentially be performed with the developed real-time MRI guidance strategy. Whilst tracking optimisation is vital it seems prudent to concomitantly focus on MLC strategies and further treatment planning studies. Dynamic MLC investigations will help to elucidate whether the proposed strategy is mechanically feasible while additional treatment planning studies will give further insight into tracking accuracy magnitudes that may be required for a more general population. Investigations into treatment plan delivery on a linac with a programmable motion platform and the dynamic MLC tracking should be conducted in future experiments.

5.3.3 MRI-Linac cardiac radiosurgery

The aim of this thesis was to analyse and improve the existing tracking method which was initially developed to provide real-time target information and could be incorporated as part

of a gated or tracked motion compensation strategy. The results of this thesis further validate previous assumptions and warrant ongoing investigation of the new approach. Furthermore, the virtual study highlights areas of the project that should be of immediate future focus and areas that are of less prompt importance. Overall, the results of this work further demonstrate that a non-invasive radiosurgical treatment for AF could potentially be performed in an integrated MRI-Linac with real-time guidance.

6

CONCLUSION

The aim of this thesis was to quantify and advance a recently developed non-invasive real-time image-guided treatment for atrial fibrillation (AF) using an integrated MRI linear accelerator (MRI-Linac). The 4 dimensional extended cardiac-torso (XCAT) phantom software is used for this purpose due to an unavailability of 4D real-time anatomical magnetic resonance imaging (MRI) data. The XCAT phantom allows realistic anthropomorphic anatomy and physiology to be simulated for MRI imaging research.

The existing tracking methodology was successfully quantified to have a tracking error of 0.6 mm for a highly detailed digital simulation. This represented a perfect and thus unrealistic scenario. The quantification was extended with simulations closely resembling the real-world procedure. Here, a 3D mean tracking error closely representative of the original tracking methodology was found to be 3.2 ± 1.7 mm. After tracking developments were applied, the best resultant tracking function produced a mean 3D tracking error of 2.9 ± 1.6 mm. These results strongly agree with the 2D tracking errors from the previous study where it was inferred that the mean 3D tracking error was 3 - 4 mm. Furthermore, a first look at how a patient's unique anatomy and physiology affects tracking accuracy is investigated. A patient's heart rate is the most influential anatomical parameter on tracking accuracy tested here. Comparing best performing tracking functions across the virtual patients show that the optimal tracking function is patient-specific.

From the previous investigation, a motion compensation strategy that can achieve margins of less than 5 mm could be considered feasible according to the treatment planning study conducted on an ideal patient. The tracking errors to date demonstrate this is achievable. If the real-time image-guidance method presented here is to be used in an MRI-Linac environment treatment deliverance would need an accuracy of less than 1 mm. This has been

reported with dynamic multi-leaf collimator (MLC) tracking but should be tested on this unique electrocardiogram (ECG)-guided template matching method.

This thesis furthers the proof-of-principle groundwork toward an entirely non-invasive treatment of AF using a MRI-Linac with real-time image guidance. It quantifies the cardiac tracking in a scenario as close to real-world as possible and highlighs areas of development where succeeding studies should focus.

REFERENCES

[1] Abecasis, J., Dourado, R., Ferreira, A., Saraiva, C., Cavaco, D., Santos, K. R., Morgado, F. B., Adragão, P., and Silva, A. (2009). Left atrial volume calculated by multi-detector computed tomography may predict successful pulmonary vein isolation in catheter ablation of atrial fibrillation. *Europace*, 11(10):1289–1294.

[2] Ames, A. and Stevenson, W. G. (2006). Catheter ablation of atrial fibrillation. *Circulation*, 113(13):e666–e668.

[3] Badger, T. J., Daccarett, M., Akoum, N. W., Adjei-Poku, Y. A., Burgon, N. S., Haslam, T. S., Kalvaitis, S., Kuppahally, S., Vergara, G., McMullen, L., et al. (2010). Evaluation of left atrial lesions after initial and repeat atrial fibrillation ablation lessons learned from delayed-enhancement mri in repeat ablation procedures. *Circulation: Arrhythmia and Electrophysiology*, 3(3):249–259.

[4] Ballester, M. A. G., Zisserman, A. P., and Brady, M. (2002). Estimation of the partial volume effect in mri. *Medical Image Analysis*, 6(4):389–405.

[5] Benjamin, E. J., Wolf, P. A., D'Agostino, R. B., Silbershatz, H., Kannel, W. B., and Levy, D. (1998). Impact of atrial fibrillation on the risk of death the framingham heart study. *Circulation*, 98(10):946–952.

[6] Bjerre, T., Crijns, S., af Rosenschöld, P. M., Aznar, M., Specht, L., Larsen, R., and Keall, P. (2013). Three-dimensional mri-linac intra-fraction guidance using multiple orthogonal cine-mri planes. *Physics in medicine and biology*, 58(14):4943.

[7] Blanck, O., Bode, F., Gebhard, M., Hunold, P., Brandt, S., Bruder, R., Grossherr, M., Vonthein, R., Rades, D., and Dunst, J. (2014). Dose-escalation study for cardiac radiosurgery in a porcine model. *International Journal of Radiation Oncology* Biology* Physics*, 89(3):590–598.

[8] Boda-Heggemann, J., Walter, C., Rahn, A., Wertz, H., Loeb, I., Lohr, F., and Wenz, F. (2006). Repositioning accuracy of two different mask systems—3d revisited: comparison using true 3d/3d matching with cone-beam ct. *International Journal of Radiation Oncology* Biology* Physics*, 66(5):1568–1575.

[9] Bode, F., Blanck, O., Gebhard, M., Hunold, P., Grossherr, M., Brandt, S., Vonthein, R., Thiele, H., Dunst, J., and Rades, D. (2015). Pulmonary vein isolation by radiosurgery: implications for non-invasive treatment of atrial fibrillation. *Europace*, 17(12):1868–1874.

[10] Bortfeld, T., Schmidt-Ullrich, R., De Neve, W., and Wazer, D. E. (2006). *Image-guided IMRT*, volume 18. Cambridge Univ Press.

[11] Brass, L. M., Krumholz, H. M., Scinto, J. M., and Radford, M. (1997). Warfarin use among patients with atrial fibrillation. *Stroke*, 28(12):2382–2389.

[12] Brix, L., Ringgaard, S., Sørensen, T. S., and Poulsen, P. R. (2014). Three-dimensional liver motion tracking using real-time two-dimensional mri. *Medical physics*, 41(4):042302.

[13] Buch, P., Friberg, J., Scharling, H., Lange, P., and Prescott, E. (2003). Reduced lung function and risk of atrial fibrillation in the copenhagen city heart study. *European Respiratory Journal*, 21(6):1012–1016.

[14] Cai, J., Chang, Z., Wang, Z., Segars, W. P., and Yin, F.-F. (2011). Four-dimensional magnetic resonance imaging (4d-mri) using image-based respiratory surrogate: a feasibility study. *Medical physics*, 38(12):6384–6394.

[15] Camm, A. J., Kirchhof, P., Lip, G. Y., Schotten, U., Savelieva, I., Ernst, S., Van Gelder, I. C., Al-Attar, N., Hindricks, G., Prendergast, B., et al. (2010). Guidelines for the management of atrial fibrillation. *European heart journal*, 31(19):2369–2429.

[16] Cappato, R., Calkins, H., Chen, S.-A., Davies, W., Iesaka, Y., Kalman, J., Kim, Y.-H., Klein, G., Packer, D., and Skanes, A. (2005). Worldwide survey on the methods, efficacy, and safety of catheter ablation for human atrial fibrillation. *Circulation*, 111(9):1100–1105.

[17] Chang, S. D., Main, W., Martin, D. P., Gibbs, I. C., and Heilbrun, M. P. (2003). An analysis of the accuracy of the cyberknife: a robotic frameless stereotactic radiosurgical system. *Neurosurgery*, 52(1):140–147.

[18] CHSS (2016). Diagnosis and treatment of atrial fibrillation. http://www.chss.org.uk/heart-information-and-support/about-your-heart-condition/common-heart-conditions/heart-arrhythmias-2/medical-treatment-atrial-fibrillation/.

[19] Cvek, J., Neuwirth, R., Knybel, L., Molenda, L., Otahal, B., Pindor, J., Murárová, M., Kodaj, M., Fiala, M., Branny, M., et al. (2014). Cardiac radiosurgery for malignant ventricular tachycardia. *Cureus*, 6(7).

[20] Delaney, G., Jacob, S., Featherstone, C., and Barton, M. (2005). The role of radiotherapy in cancer treatment. *Cancer*, 104(6):1129–1137.

[21] Depa, M., Sabuncu, M. R., Holmvang, G., Nezafat, R., Schmidt, E. J., and Golland, P. (2010). Robust atlas-based segmentation of highly variable anatomy: Left atrium segmentation. In *STACOM/CESC*, pages 85–94. Springer.

[22] Fallone, B. G. (2014). The rotating biplanar linac–magnetic resonance imaging system. In *Seminars in radiation oncology*, volume 24, pages 200–202. Elsevier.

[23] Ganong, W. F. and Barrett, K. E. (1995). *Review of medical physiology*. Appleton & Lange Norwalk, CT.

[24] Ge, Y., O'Brien, R. T., Shieh, C.-C., Booth, J. T., and Keall, P. J. (2014). Toward the development of intrafraction tumor deformation tracking using a dynamic multi-leaf collimator. *Medical physics*, 41(6):061703.

[25] Go, A. S., Hylek, E. M., Phillips, K. A., Chang, Y., Henault, L. E., Selby, J. V., and Singer, D. E. (2001). Prevalence of diagnosed atrial fibrillation in adults: national implications for rhythm management and stroke prevention: the anticoagulation and risk factors in atrial fibrillation (atria) study. *Jama*, 285(18):2370–2375.

[26] Goldman, L. W. (2008). Principles of ct: multislice ct. *Journal of nuclear medicine technology*, 36(2):57–68.

[27] Gudbjartsson, H. and Patz, S. (1995). The rician distribution of noisy mri data. *Magnetic resonance in medicine*, 34(6):910–914.

[28] Haïssaguerre, M., Jaïs, P., Shah, D. C., Garrigue, S., Takahashi, A., Lavergne, T., Hocini, M., Peng, J. T., Roudaut, R., and Clémenty, J. (2000). Electrophysiological end point for catheter ablation of atrial fibrillation initiated from multiple pulmonary venous foci. *Circulation*, 101(12):1409–1417.

[29] Haissaguerre, M., Jaïs, P., Shah, D. C., Takahashi, A., Hocini, M., Quiniou, G., Garrigue, S., Le Mouroux, A., Le Métayer, P., and Clémenty, J. (1998). Spontaneous initiation of atrial fibrillation by ectopic beats originating in the pulmonary veins. *New England Journal of Medicine*, 339(10):659–666.

[30] Hartzog, K. (2016). The cardiovascular system. http://www.starsandseas.com/sas

[31] Hof, I., Chilukuri, K., ARBAB-ZADEH, A., Scherr, D., Dalal, D., Nazarian, S., Henrikson, C., Spragg, D., Berger, R., Marine, J., et al. (2009). Does left atrial volume and pulmonary venous anatomy predict the outcome of catheter ablation of atrial fibrillation? *Journal of cardiovascular electrophysiology*, 20(9):1005–1010.

[32] Hohnloser, S. H., Kuck, K.-H., Lilienthal, J., Investigators, P., et al. (2000). Rhythm or rate control in atrial fibrillation—pharmacological intervention in atrial fibrillation (piaf): a randomised trial. *The Lancet*, 356(9244):1789–1794.

[33] Hudsmith, L. E., Petersen, S. E., Francis, J. M., Robson, M. D., and Neubauer, S. (2005). Normal human left and right ventricular and left atrial dimensions using steady state free precession magnetic resonance imaging. *Journal of cardiovascular magnetic resonance*, 7(5):775–782.

[34] Ipsen, S. (2015). Radiotherapy beyond cancer: Motion analysis, treatment planning and real-time target localization for non-invasive cardiac radiosurgery with mri guidance. Unpublished thesis.

[35] Ipsen, S., Blanck, O., Oborn, B., Bode, F., Liney, G., Hunold, P., Rades, D., Schweikard, A., and Keall, P. (2014). Radiotherapy beyond cancer: Target localization in real-time mri and treatment planning for cardiac radiosurgery. *Medical physics*, 41(12):120702.

[36] Jaffray, D. A., Carlone, M. C., Milosevic, M. F., Breen, S. L., Stanescu, T., Rink, A., Alasti, H., Simeonov, A., Sweitzer, M. C., and Winter, J. D. (2014). A facility for magnetic resonance–guided radiation therapy. In *Seminars in radiation oncology*, volume 24, pages 193–195. Elsevier.

[37] Järvinen, V. M., Kupari, M. M., Poutanen, V.-P., and Hekali, P. E. (1996). A simplified method for the determination of left atrial size and function using cine magnetic resonance imaging. *Magnetic resonance imaging*, 14(3):215–226.

[38] Keall, P. J., Barton, M., Crozier, S., et al. (2014). The australian magnetic resonance imaging–linac program. In *Seminars in radiation oncology*, volume 24, pages 203–206. Elsevier.

[39] Lagendijk, J. J., Raaymakers, B. W., and van Vulpen, M. (2014). The magnetic resonance imaging–linac system. In *Seminars in radiation oncology*, volume 24, pages 207–209. Elsevier.

[40] Larsson, B. (1996). *The history of radiosurgery: the early years (1950–1970)*. Karger Publishers.

[41] Lee, D., Greer, P. B., Ludbrook, J., Arm, J., Hunter, P., Pollock, S., Makhija, K., O'brien, R. T., Kim, T., and Keall, P. (2015). Audiovisual biofeedback improves cine-mri measured lung tumor motion consistency. *International Journal of Radiation Oncology* Biology* Physics*.

[42] Lickfett, L., Dickfeld, T., Kato, R., Tandri, H., Vasamreddy, C. R., Berger, R., Bluemke, D., Lüderitz, B., Halperin, H., and Calkins, H. (2005). Changes of pulmonary vein orifice size and location throughout the cardiac cycle: dynamic analysis using magnetic resonance cine imaging. *Journal of cardiovascular electrophysiology*, 16(6):582–588.

[43] Lloyd-Jones, D. M., Wang, T. J., Leip, E. P., Larson, M. G., Levy, D., Vasan, R. S., D'Agostino, R. B., Massaro, J. M., Beiser, A., Wolf, P. A., et al. (2004). Lifetime risk for development of atrial fibrillation the framingham heart study. *Circulation*, 110(9):1042–1046.

[44] Loo, B. W., Soltys, S. G., Wang, L., Lo, A., Fahimian, B. P., Iagaru, A., Norton, L., Shan, X., Gardner, E., Fogarty, T., et al. (2015). Stereotactic ablative radiotherapy for the treatment of refractory cardiac ventricular arrhythmia. *Circulation: Arrhythmia and Electrophysiology*, 8(3):748–750.

[45] Lutomsky, B. A., Rostock, T., Koops, A., Steven, D., Müllerleile, K., Servatius, H., Drewitz, I., Ueberschär, D., Plagemann, T., Ventura, R., et al. (2008). Catheter ablation of paroxysmal atrial fibrillation improves cardiac function: a prospective study on the impact of atrial fibrillation ablation on left ventricular function assessed by magnetic resonance imaging. *Europace*, 10(5):593–599.

[46] Maceira, A. M., Cosín-Sales, J., Roughton, M., Prasad, S. K., and Pennell, D. J. (2010). Reference left atrial dimensions and volumes by steady state free precession cardiovascular magnetic resonance. *Journal of Cardiovascular Magnetic Resonance*, 12(1):65.

[47] Maguire, P. J., Gardner, E., Jack, A. B., Zei, P., Al-Ahmad, A., Fajardo, L., Ladich, E., and Takeda, P. (2011). Cardiac radiosurgery (cyberheart™) for treatment of arrhythmia: Physiologic and histopathologic correlation in the porcine model. *Cureus*, 3(8).

[48] Mathers, C. D. and Loncar, D. (2006). Projections of global mortality and burden of disease from 2002 to 2030. *Plos med*, 3(11):e442.

[49] McLeish, K., Hill, D. L., Atkinson, D., Blackall, J. M., and Razavi, R. (2002). A study of the motion and deformation of the heart due to respiration. *Medical Imaging, IEEE Transactions on*, 21(9):1142–1150.

[50] Miyasaka, Y., Barnes, M. E., Gersh, B. J., Cha, S. S., Bailey, K. R., Abhayaratna, W. P., Seward, J. B., and Tsang, T. S. (2006). Secular trends in incidence of atrial fibrillation in olmsted county, minnesota, 1980 to 2000, and implications on the projections for future prevalence. *Circulation*, 114(2):119–125.

[51] Morady, F. and Zipes, D. (2012). Atrial fibrillation: Clinical features, mechanisms, and management. *Braunwald's Heart Disease: A Textbook of Cardiovascular Medicine,*, 1:825–844.

[52] Mukaka, M. (2012). A guide to appropriate use of correlation coefficient in medical research. *Malawi Medical Journal*, 24(3):69–71.

[53] NLM (2015). The visible human project. www.nlm.nih.gov/research/visible/getting_data.html.

[54] Paganelli, C., Lee, D., Greer, P. B., Baroni, G., Riboldi, M., and Keall, P. (2015). Quantification of lung tumor rotation with automated landmark extraction using orthogonal cine mri images. *Physics in medicine and biology*, 60(18):7165.

[55] Page, R. L. and Roden, D. M. (2005). Drug therapy for atrial fibrillation: where do we go from here? *Nature Reviews Drug Discovery*, 4(11):899–910.

[56] Park, J., Metaxas, D., Young, A. A., and Axel, L. (1996). Deformable models with parameter functions for cardiac motion analysis from tagged mri data. *Medical Imaging, IEEE Transactions on*, 15(3):278–289.

[57] Patel, A. R., Fatemi, O., Norton, P. T., West, J. J., Helms, A. S., Kramer, C. M., and Ferguson, J. D. (2008). Cardiac cycle–dependent left atrial dynamics: Implications for catheter ablation of atrial fibrillation. *Heart Rhythm*, 5(6):787–793.

[58] Pham, Q., Vincent, F., Clarysse, P., Croisille, P., and Magnin, I. (2001). A fem-based deformable model for the 3d segmentation and tracking of the heart in cardiac mri. In *Image and Signal Processing and Analysis, 2001. ISPA 2001. Proceedings of the 2nd International Symposium on*, pages 250–254. IEEE.

[59] Richa, R., Poignet, P., and Liu, C. (2008). Deformable motion tracking of the heart surface. In *Intelligent Robots and Systems, 2008. IROS 2008. IEEE/RSJ International Conference on*, pages 3997–4003. IEEE.

[60] Schaerer, J., Casta, C., Pousin, J., and Clarysse, P. (2010). A dynamic elastic model for segmentation and tracking of the heart in mr image sequences. *Medical Image Analysis*, 14(6):738–749.

[61] Schotten, U., Verheule, S., Kirchhof, P., and Goette, A. (2011). Pathophysiological mechanisms of atrial fibrillation: a translational appraisal. *Physiological reviews*, 91(1):265–325.

[62] Segars, W., Sturgeon, G., Mendonca, S., Grimes, J., and Tsui, B. M. (2010). 4d xcat phantom for multimodality imaging research. *Medical physics*, 37(9):4902–4915.

[63] Segars, W. P. and Tsui, B. M. (2009). Mcat to xcat: The evolution of 4-d computerized phantoms for imaging research. *Proceedings of the IEEE*, 97(12):1954–1968.

[64] Seregni, M., Paganelli, C., Lee, D., Greer, P., Baroni, G., Keall, P., and Riboldi, M. (2016). Motion prediction in mri-guided radiotherapy based on interleaved orthogonal cine-mri. *Physics in medicine and biology*, 61(2):872.

[65] Sharma, A., Wong, D., Weidlich, G., Fogarty, T., Jack, A., Sumanaweera, T., and Maguire, P. (2010). Noninvasive stereotactic radiosurgery (cyberheart) for creation of ablation lesions in the atrium. *Heart Rhythm*, 7(6):802–810.

[66] Solberg, T. D., Siddon, R. L., and Kavanagh, B. (2012). Historical development of stereotactic ablative radiotherapy. In *Stereotactic Body Radiation Therapy*, pages 9–35. Springer.

[67] Teo, B., Dieterich, S., Blanck, O., Sumanaweera, T., and Gardner, E. (2009). Su-ff-t-559: Effect of cardiac motion on the cyberknife synchrony tracking system for radiosurgical cardiac ablation. *Medical Physics*, 36(6):2653–2653.

[68] Tobon-Gomez, C., Sukno, F., Bijnens, B., Huguet, M., and Frangi, A. (2011). Realistic simulation of cardiac magnetic resonance studies modeling anatomical variability, trabeculae, and papillary muscles. *Magnetic Resonance in Medicine*, 65(1):280–288.

[69] Tryggestad, E., Flammang, A., Hales, R., Herman, J., Lee, J., McNutt, T., Roland, T., Shea, S. M., and Wong, J. (2013). 4d tumor centroid tracking using orthogonal 2d dynamic mri: Implications for radiotherapy planning. *Medical physics*, 40(9):091712.

[70] Tsang, T. S., Barnes, M. E., Bailey, K. R., Leibson, C. L., Montgomery, S. C., Takemoto, Y., Diamond, P. M., Marra, M. A., Gersh, B. J., Wiebers, D. O., et al. (2001). Left atrial volume: important risk marker of incident atrial fibrillation in 1655 older men and women. In *Mayo Clinic Proceedings*, volume 76, pages 467–475. Elsevier.

[71] UCDavis (2016). Cardiac cycle: Ventricular diastole. http://biowiki.ucdavis.edu/@api/deki/files/2978/2028-cardiac-cycle-vs-electrocardiogram.jpg?revision=1.

[72] UCLA (2016). Introduction to nurbs modeling. http://users.design.ucla.edu/ cariesta/mayacoursenotes/html/body_modeling_basics.html.

[73] Uecker, M., Zhang, S., Voit, D., Karaus, A., Merboldt, K.-D., and Frahm, J. (2010). Real-time mri at a resolution of 20 ms. *NMR in Biomedicine*, 23(8):986–994.

[74] Veress, A. I., Segars, W. P., Tsui, B. M., and Gullber, G. T. (2011). Incorporation of a left ventricle finite element model defining infarction into the xcat imaging phantom. *Medical Imaging, IEEE Transactions on*, 30(4):915–927.

[75] Vignaux, O. B., Augui, J., Coste, J., Argaud, C., Le Roux, P., Carlier, P. G., Duboc, D., and Legmann, P. (2001). Comparison of single-shot fast spin-echo and conventional spin-echo sequences for mr imaging of the heart: Initial experience 1. *Radiology*, 219(2):545–550.

[76] Whelan, B., Gierman, S., Holloway, L., Schmerge, J., Keall, P., and Fahrig, R. (2016). A novel electron accelerator for mri-linac radiotherapy. *Medical physics*, 43(3):1285–1294.

[77] Wissmann, L., Santelli, C., Segars, W. P., and Kozerke, S. (2014). Mrxcat: Realistic numerical phantoms for cardiovascular magnetic resonance. *J Cardiovasc Magn Reson*, 16:63.

[78] Wolf, P. A., Abbott, R. D., and Kannel, W. B. (1991). Atrial fibrillation as an independent risk factor for stroke: the framingham study. *Stroke*, 22(8):983–988.

[79] Wyse, D., Waldo, A., DiMarco, J., Domanski, M., Rosenberg, Y., Schron, E., Kellen, J., Greene, H., Mickel, M., Dalquist, J., et al. (2002). A comparison of rate control and rhythm control in patients with atrial fibrillation. *N Engl J Med*, 347(23):1825–33.

[80] Yu, C., Main, W., Taylor, D., Kuduvalli, G., Apuzzo, M. L., Adler Jr, J. R., and Wang, M. Y. (2004). An anthropomorphic phantom study of the accuracy of cyberknife spinal radiosurgery. *Neurosurgery*, 55(5):1138–1149.

[81] Zhang, Y., Ren, L., Ling, C. C., and Yin, F.-F. (2013). Respiration-phase-matched digital tomosynthesis imaging for moving target verification: A feasibility study. *Medical physics*, 40(7):071723.

[82] Zhong, H., Kim, J., and Chetty, I. J. (2010). Analysis of deformable image registration accuracy using computational modeling. *Medical physics*, 37(3):970–979.

Appendix A

XCAT virtual patient study template matching results

Table A.1 Mean error and the three anatomical directional error for the 'dual last position' (DLP) template matching function

	Template matching method - DLP function							
	Sys/max-dia RMS error (mm)				**Sys/end-dia RMS error (mm)**			
Patient	SI	AP	LR	**3D**	SI	AP	LR	**3D**
1	2.7	0.2	1.0	**2.9**	0.8	2.0	4.6	**5.1**
2	1.6	0.7	1.8	**2.5**	0.2	1.0	5.6	**5.6**
3	2.2	2.9	3.5	**5.0**	5.1	7.0	11.4	**14.4**
4	1.1	1.6	0.7	**2.1**	4.2	4.2	6.5	**8.8**
5	4.4	3.9	4.9	**7.6**	4.4	5.1	10.1	**12.1**
6	0.5	0.1	1.2	**1.3**	1.9	2.5	3.3	**4.5**
7	0.3	1.4	0.6	**2.5**	8.3	5.3	4.0	**10.7**
8	1.1	1.5	0.1	**1.9**	1.5	2.5	10.5	**10.9**
9	4.3	3.2	2.9	**6.1**	3.1	4.5	5.7	**7.9**
10	0.2	0.4	4.2	**4.2**	2.8	0.6	9.6	**10.0**
11	1.7	2.0	1.1	**2.8**	0.5	2.2	0.5	**2.3**
12	1.9	1.4	0.4	**2.4**	1.0	2.0	3.2	**4.0**
13	0.2	1.5	1.3	**2.0**	5.7	6.0	8.5	**11.9**
14	1.8	0.6	1.7	**2.5**	1.3	2.6	3.5	**4.6**
15	3.1	2.1	4.6	**6.0**	0.9	2.9	2.1	**3.7**
16	4.2	4.3	7.0	**9.3**	5.9	5.0	13.2	**15.3**
17	2.0	0.7	2.1	**3.0**	1.4	1.6	5.8	**6.2**
18	2.2	2.1	2.3	**3.8**	4.6	1.8	4.5	**6.7**
19	0.9	0.4	1.1	**1.5**	4.6	3.8	8.3	**10.2**
20	2.4	0.1	1.7	**3.0**	1.8	0.6	2.3	**3.0**
Mean	1.9	1.6	2.2	**3.6**	3.0	3.2	6.2	**7.9**
± std	± 1.3	± 1.2	± 1.8	**± 2.1**	± 2.2	± 1.8	± 3.5	**± 3.9**

Table A.2 Mean error and the three anatomical directional error for the 'dual all positions' (DAP) template matching function.

	Template matching method - DAP function							
	Sys/max-dia RMS error (mm)				**Sys/end-dia RMS error (mm)**			
Patient	SI	AP	LR	**3D**	SI	AP	LR	**3D**
1	1.0	0.7	4.2	**4.4**	3.5	0.6	3.5	**5.0**
2	0.6	1.2	4.5	**4.7**	0.4	0.3	2.3	**2.3**
3	0.7	2.7	10.1	**10.5**	1.2	0.6	2.4	**2.8**
4	0.5	1.4	0.4	**1.5**	3.0	1.2	2.4	**4.1**
5	0.8	0.3	9.6	**9.6**	2.5	1.5	3.9	**4.9**
6	1.2	0.5	0.5	**1.4**	2.0	0.3	0.7	**2.1**
7	2.0	2.3	4.5	**5.5**	4.5	0.6	3.1	**5.5**
8	0.5	0.5	7.0	**7.0**	5.1	4.3	2.8	**7.2**
9	1.4	1.6	6.2	**6.5**	0.8	0.1	14.5	**14.5**
10	1.6	0.3	6.5	**6.7**	1.2	0.3	4.5	**4.7**
11	0.6	1.4	4.1	**4.4**	1.3	1.7	3.6	**4.1**
12	1.7	1.5	3.9	**4.5**	0.5	3.0	0.0	**3.0**
13	0.9	1.8	3.4	**4.0**	3.0	0.7	5.0	**5.9**
14	1.0	0.4	1.5	**1.8**	0.4	0.5	1.0	**1.2**
15	1.0	2.3	7.2	**7.6**	3.1	1.2	2.5	**4.2**
16	1.0	2.4	15.4	**15.6**	1.7	0.5	6.2	**6.5**
17	0.2	1.2	7.0	**7.1**	1.2	0.5	2.9	**3.2**
18	0.4	0.6	1.0	**1.2**	3.6	0.3	1.5	**3.9**
19	1.6	0.1	0.3	**1.6**	1.0	1.3	0.0	**1.7**
20	1.2	0.1	2.0	**2.2**	2.4	1.1	3.3	**4.2**
Mean	1.0	1.2	5.0	**5.4**	2.1	1.0	3.3	**4.6**
± std	± 0.5	± 0.8	± 3.8	**± 3.6**	± 1.4	± 1.0	± 3.1	**± 2.8**

Table A.3 Mean error and the three anatomical directional error for the 'dual last position bordered' (DLPB) template matching function.

	Template matching method - DLPB function Sys/max-dia RMS error (mm)			
Patient	SI	AP	LR	**3D**
1	1.7	2.1	1.4	**3.1**
2	3.6	0.3	0.5	**3.6**
3	2.2	2.8	3.8	**5.2**
4	1.2	1.5	0.5	**2.0**
5	0.7	0.6	5.6	**5.7**
6	1.4	0.1	1.4	**2.0**
7	0.1	2.3	0.7	**2.4**
8	0.5	1.6	1.2	**2.1**
9	1.1	1.7	3.8	**4.3**
10	0.7	2.6	2.2	**3.5**
11	1.5	1.9	0.7	**2.5**
12	0.0	0.4	0.1	**0.4**
13	0.7	1.9	1.5	**2.5**
14	1.8	0.4	1.8	**2.6**
15	1.2	2.0	3.1	**3.9**
16	2.6	2.6	7.1	**8.0**
17	0.4	1.7	2.3	**2.9**
18	0.7	0.9	3.0	**3.2**
19	0.8	0.6	0.7	**1.2**
20	2.8	0.3	2.2	**2.9**
Mean ± std	1.3 ± 0.9	1.4 ± 0.9	2.2 ± 1.8	**3.2 ± 1.7**

Table A.4 Mean error and the three anatomical directional error for the 'dual all positions bordered' (DAPB) template matching function.

	Template matching method - DAPB function							
	Sys/max-dia RMS error (mm)				**Sys/end-dia RMS error (mm)**			
Patient	SI	AP	LR	**3D**	SI	AP	LR	**3D**
1	1.1	0.6	0.1	**1.3**	1.2	2.9	2.9	**3.2**
2	0.4	1.0	0.8	**1.3**	2.3	1.4	1.4	**3.2**
3	0.6	2.6	10.0	**10.3**	1.7	4.0	4.0	**5.9**
4	0.8	2.5	0.4	**2.6**	0.2	2.3	4.6	**5.1**
5	0.0	1.0	2.6	**2.8**	0.3	1.2	2.9	**3.2**
6	0.3	0.1	0.5	**0.6**	1.5	0.8	0.3	**1.8**
7	2.0	2.0	4.3	**5.2**	1.6	1.8	2.6	**3.5**
8	0.0	0.0	1.1	**1.1**	2.2	1.8	4.0	**4.9**
9	0.2	1.6	2.5	**3.0**	0.3	1.0	3.7	**4.2**
10	1.1	2.8	0.4	**3.1**	1.4	3.3	3.8	**5.2**
11	0.6	2.6	0.8	**2.8**	0.1	3.1	2.8	**4.2**
12	0.5	1.4	2.2	**2.6**	0.6	1.1	1.9	**2.3**
13	0.3	2.3	1.0	**2.5**	0.3	2.7	1.1	**2.9**
14	0.3	0.6	3.1	**3.2**	0.3	1.2	1.1	**1.7**
15	0.3	2.9	9.8	**10.3**	0.1	3.2	5.6	**6.5**
16	2.4	2.9	5.7	**6.8**	1.9	3.9	6.2	**7.6**
17	1.3	1.9	0.5	**2.4**	1.5	2.4	3.9	**4.9**
18	0.1	0.4	2.2	**2.2**	2.0	1.9	1.6	**3.2**
19	1.5	0.0	3.4	**3.7**	1.0	0.6	0.4	**1.3**
20	0.5	0.1	1.5	**1.6**	1.0	0.6	5.9	**6.0**
Mean	0.7	1.5	2.6	**3.5**	1.1	2.1	3.0	**4.0**
± std	± 0.7	± 1.1	± 2.9	**± 2.7**	± 0.8	± 1.1	± 1.8	**± 1.7**

Table A.5 Mean error and the three anatomical directional error for the 'dual last position dynamic bordered' (DLPDB) and 'dual all positions dynamic bordered' (DAPDB) template matching functions.

	Template matching method							
	DLPDB RMS error (mm)				**DAPDB RMS error (mm)**			
Patient	SI	AP	LR	**3D**	SI	AP	LR	**3D**
1	1.4	1.9	0.4	**2.5**	1.6	2.3	0.2	**2.8**
2	3.6	0.6	0.9	**3.8**	0.4	1.0	1.3	**1.7**
3	2.2	2.8	3.8	**5.2**	1.1	2.5	5.4	**6.0**
4	1.4	1.5	0.2	**2.0**	1.0	2.1	0.2	**2.3**
5	0.6	0.8	5.1	**5.2**	1.3	1.1	4.9	**5.2**
6	1.5	0.0	0.9	**1.8**	2.1	1.9	0.9	**3.0**
7	0.1	2.3	0.9	**2.4**	0.2	1.9	0.4	**2.0**
8	0.3	1.8	1.5	**2.3**	1.3	1.5	0.1	**2.0**
9	1.1	1.7	3.9	**4.4**	1.0	1.7	4.6	**5.0**
10	0.6	2.6	1.8	**3.2**	0.2	2.9	0.1	**2.9**
11	1.1	2.2	0.5	**2.6**	0.4	1.9	0.4	**1.9**
12	0.1	0.4	0.1	**0.4**	0.5	1.7	1.4	**2.3**
13	0.7	1.9	1.5	**2.5**	0.5	2.1	0.3	**2.2**
14	2.0	0.5	1.0	**2.3**	1.1	0.4	0.0	**1.2**
15	1.2	2.0	3.3	**4.0**	0.5	2.2	6.7	**7.1**
16	2.8	2.6	7.0	**8.0**	0.9	2.0	1.3	**2.6**
17	0.6	1.8	1.9	**2.7**	0.1	2.0	0.9	**2.2**
18	0.4	0.7	2.9	**3.0**	1.2	0.5	0.9	**1.6**
19	0.8	0.6	0.8	**1.3**	1.5	0.1	2.4	**2.8**
20	2.8	0.1	1.0	**2.9**	0.7	0.1	0.5	**0.9**
Mean ± std	1.3 ± 1.0	1.4 ± 0.9	2.0 ± 1.8	**3.1 ± 1.7**	0.9 ± 0.5	1.6 ± 0.8	1.6 ± 2.0	**2.9 ± 1.6**

Table A.6 Mean error and the three anatomical directional error for the 'dual last position dynamic bordered' (DLPDB) and 'dual all positions dynamic bordered' (DAPDB) template matching methods which incorporate the isolated template function.

	Template matching method - Isolated template function							
	DLPDB RMS error (mm)				**DAPDB RMS error (mm)**			
Patient	SI	AP	LR	**3D**	SI	AP	LR	**3D**
1	3.3	0.5	12.0	**12.5**	1.6	2.3	0.2	**2.8**
2	1.1	0.2	8.4	**8.4**	0.4	1.0	1.3	**1.7**
3	10.0	11.0	23.0	**27.5**	1.1	2.5	5.4	**6.0**
4	2.1	0.2	7.2	**7.5**	1.0	2.1	0.2	**2.3**
5	13.0	3.3	29.8	**32.6**	1.3	1.1	4.9	**5.2**
Mean	5.9	3.0	16.1	**17.7**	4.9	1.2	30.3	**31.1**
± std	± 5.3	± 4.6	± 9.9	**± 11.6**	± 5.0	± 0.8	± 12.7	**± 12.5**

Table A.7 Mean error and the three anatomical directional error for the 'tri-last position' (TLP) and 'tri-all positions' (TAP) template matching functions.

	Template matching method - Tri- (Sys/MD/ED)							
	TLP RMS error (mm)				**TAP RMS error (mm)**			
Patient	SI	AP	LR	**3D**	SI	AP	LR	**3D**
1	0.6	2.1	2.7	**3.5**	1.1	2.7	1.2	**3.1**
2	2.6	0.8	2.4	**3.7**	2.2	1.3	0.7	**2.6**
3	0.5	3.8	0.2	**3.9**	1.7	4.2	2.5	**5.2**
4	1.0	1.8	2.6	**3.3**	0.3	2.3	5.5	**6.0**
5	0.1	0.9	3.0	**3.2**	0.6	1.4	2.7	**3.1**
6	2.5	0.2	4.0	**4.7**	5.4	2.0	3.3	**6.7**
7	0.8	2.0	4.7	**5.1**	1.2	1.9	5.6	**6.3**
8	0.3	2.3	3.2	**3.9**	3.5	1.4	1.0	**3.9**
9	0.4	1.8	1.2	**2.1**	0.5	2.1	1.8	**2.7**
10	1.1	2.5	1.6	**3.2**	1.7	3.3	1.5	**4.0**
11	2.3	2.6	4.8	**6.0**	0.3	3.0	0.6	**3.1**
12	1.1	1.9	1.9	**2.9**	0.7	1.4	1.3	**2.0**
13	0.2	2.7	0.2	**2.8**	0.3	3.3	2.1	**3.9**
14	1.4	0.7	1.7	**2.3**	0.3	1.0	3.9	**4.0**
15	0.4	2.5	2.5	**3.6**	1.0	3.0	2.6	**4.1**
16	1.2	3.2	0.6	**3.5**	1.6	3.1	0.6	**3.5**
17	1.0	1.3	0.9	**1.9**	1.7	2.3	1.8	**3.4**
18	1.3	2.2	3.0	**3.9**	2.1	1.8	7.3	**7.8**
19	1.6	0.3	0.6	**1.7**	0.9	0.4	0.9	**1.4**
20	3.5	0.3	4.1	**5.4**	1.0	0.4	2.6	**2.8**
Mean	1.2	1.8	2.3	**3.5**	1.4	2.1	2.5	**4.0**
± std	± 0.9	± 1.0	± 1.4	**± 1.1**	± 1.2	± 1.0	± 1.8	**± 1.6**

Table A.8 Mean error and the three anatomical directional error for the 4D template matching and 2D plus time methods using dynamic-search bordered function.

	Template matching method							
	2D + time RMS error (mm)				**4D RMS error (mm)**			
Patient	SI	AP	LR	**3D**	SI	AP	LR	**3D**
1	0.7	0.2	1.5	**1.7**	0.8	0.3	0.7	**1.1**
2	0.3	0.6	1.1	**1.3**	0.1	0.9	1.4	**1.7**
3	0.3	3.1	2.5	**4.0**	1.6	3.1	3.8	**5.2**
4	0.3	2.0	2.0	**2.8**	0.6	2.2	0.6	**2.4**
5	2.6	2.9	7.5	**8.5**	0.6	1.6	6.2	**6.4**
6	0.3	0.5	3.0	**3.1**	0.1	0.1	0.8	**0.8**
7	0.7	2.3	3.4	**4.2**	0.8	2.1	3.6	**4.2**
8	4.9	4.1	0.6	**6.4**	0.9	2.2	0.1	**2.3**
9	3.9	1.5	5.3	**6.7**	3.3	1.9	6.0	**7.1**
10	2.0	2.4	3.6	**4.8**	2.1	2.8	2.5	**4.3**
11	0.3	1.9	3.3	**3.8**	0.5	2.9	1.8	**3.5**
12	1.2	0.5	3.2	**3.5**	0.5	1.4	3.9	**4.2**
13	0.4	2.1	3.3	**4.0**	0.6	2.7	1.6	**3.2**
14	5.0	4.0	1.4	**6.5**	0.2	0.5	1.6	**1.6**
15	0.5	2.0	5.7	**6.1**	1.7	3.5	5.0	**6.4**
16	2.0	2.8	6.8	**7.7**	2.6	3.1	4.0	**5.7**
17	0.1	1.4	3.7	**4.0**	1.4	1.8	2.7	**3.5**
18	0.8	2.0	6.5	**6.8**	0.2	1.5	0.5	**1.6**
19	1.0	0.2	0.8	**1.3**	0.8	0.4	1.0	**1.3**
20	1.5	0.1	2.3	**2.8**	0.8	0.1	1.3	**1.5**
Mean	1.4	1.8	3.4	**4.5**	1.0	1.8	2.5	**3.4**
± std	± 1.5	± 1.2	± 2.0	**± 2.1**	± 0.9	± 1.1	± 1.9	**± 2.0**

Table A.9 Mean error and the three anatomical directional error for the 'dual all positions dynamic bordered' (DAPDB) function for 2 mm^3 cardiac templates, and 2 mm^3 cardiac template, real-time images.

	Template matching method - DAPDB							
	2 mm^3 Cardiac RMS error (mm)				**2 mm^3 Cardiac and RT RMS error (mm)**			
Patient	SI	AP	LR	**3D**	SI	AP	LR	**3D**
1	1.4	1.3	0.8	**2.0**	0.3	0.6	2.2	**2.2**
2	0.1	1.2	0.3	**1.2**	0.3	1.3	0.6	**1.4**
3	0.9	1.5	4.5	**4.8**	1.0	1.4	4.6	**4.9**
4	1.5	2.2	0.8	**2.8**	2.0	2.6	2.8	**4.3**
5	1.6	1.4	5.3	**5.7**	1.8	1.4	5.5	**5.9**
6	0.6	0.4	0.0	**0.7**	0.2	0.3	1.3	**1.3**
7	0.1	2.5	0.7	**2.6**	0.4	2.3	0.5	**2.3**
8	0.6	1.7	0.8	**2.0**	0.4	1.7	1.1	**2.1**
9	1.1	1.6	4.8	**5.2**	1.1	1.3	4.6	**4.9**
10	0.9	1.1	2.0	**2.4**	0.9	1.1	1.7	**2.2**
11	0.9	2.0	2.3	**3.2**	0.5	1.8	0.1	**1.9**
12	0.3	1.6	1.1	**2.0**	0.0	2.1	0.5	**2.1**
13	0.6	2.3	0.2	**2.3**	0.8	2.2	0.1	**2.4**
14	0.3	0.6	0.4	**0.8**	0.3	0.8	1.0	**1.3**
15	2.6	2.4	2.8	**4.5**	2.6	2.4	2.6	**4.4**
16	0.2	1.5	5.9	**6.1**	1.2	2.9	4.5	**5.5**
17	0.0	1.5	0.6	**1.6**	0.4	1.6	1.0	**1.9**
18	1.6	1.6	0.8	**2.4**	1.3	1.5	0.5	**2.1**
19	0.2	0.5	1.5	**1.6**	0.3	0.3	1.8	**1.9**
20	0.6	0.5	0.4	**0.9**	0.9	0.4	0.2	**1.0**
Mean	0.8	1.5	1.8	**2.7**	0.8	1.5	1.9	**2.8**
± std	± 0.7	± 0.6	± 1.9	**± 1.7**	± 0.7	± 0.8	± 1.7	**± 1.5**

Table A.10 Mean error and the three anatomical directional error for the 4D template matching method for 2 mm^3 cardiac templates, and 2 mm^3 cardiac template, real-time images.

	Template matching method - 4D							
	2 mm^3 Cardiac RMS error (mm)				**2 mm^3 Cardiac and RT RMS error (mm)**			
Patient	SI	AP	LR	**3D**	SI	AP	LR	**3D**
1	0.4	0.9	0.1	**0.9**	0.7	0.9	0.3	**1.1**
2	0.6	1.2	0.6	**1.4**	0.9	1.2	1.1	**1.7**
3	0.2	1.5	2.3	**2.8**	0.2	1.4	1.9	**5.2**
4	1.1	2.3	1.3	**2.9**	1.8	2.4	1.8	**2.4**
5	0.6	1.6	6.2	**6.4**	2.5	1.4	8.3	**6.4**
6	0.7	0.4	0.9	**1.2**	0.6	0.3	0.7	**0.8**
7	0.2	1.7	3.4	**3.8**	0.1	1.7	3.5	**4.2**
8	2.2	2.8	2.6	**4.5**	2.4	2.9	2.7	**2.3**
9	0.3	2.3	5.4	**5.8**	0.5	2.0	5.1	**7.1**
10	0.6	0.8	2.0	**2.2**	0.4	0.6	2.4	**4.3**
11	1.0	0.8	1.1	**1.7**	0.9	1.0	2.9	**3.5**
12	0.5	1.3	4.3	**4.6**	1.1	0.6	5.6	**4.2**
13	1.1	2.8	0.9	**3.2**	1.1	2.6	2.8	**3.2**
14	0.1	1.0	0.8	**1.3**	0.5	0.8	1.5	**1.6**
15	0.3	0.3	6.3	**6.3**	1.8	0.1	6.0	**6.4**
16	0.1	1.8	3.8	**4.2**	0.1	1.1	4.2	**5.7**
17	2.4	1.8	1.9	**3.6**	0.6	2.0	1.8	**3.5**
18	0.6	1.5	2.4	**2.9**	0.8	1.3	2.4	**1.6**
19	0.1	0.2	0.9	**0.9**	0.1	0.2	0.9	**1.3**
20	0.9	0.6	3.7	**3.8**	1.0	0.4	3.8	**1.5**
Mean	0.7	1.4	2.5	**3.2**	0.9	1.2	3.0	**3.6**
± std	± 0.6	± 0.8	± 1.9	**± 1.7**	± 0.7	± 0.8	± 2.0	**± 2.0**

APPENDIX B

DIGITAL IMAGING AND COMMUNICATIONS IN MEDICINE

The Digital Imaging and Communications in Medicine (DICOM) standard was developed to assist with the connectivity of imaging systems in the handling, storing, printing and transmission of information. The DICOM standard allows imaging systems to communicate with each other even though they may store data locally using proprietary formats. Images are assigned DICOM standard header information, key elements which identify the images and related information. To ensure consistency between users and imaging modalities the key elements are defined through the DICOM data dictionary. Key elements used in this work and their descriptions are outlined in Tab.B.1. The addition of radiotherapy data to DICOM [10] will increase the connectivity between imaging and treatment modalities, with the potential to greatly assist in systems such as the MRI-Linac.

Table B.1 Digital imaging and communications in medicine (DICOM) dictionary of key elements used in this work.

DICOM key element's tag, attribute and description		
DICOM Tag	**Attribute Name**	**Description**
(0008,0032)	Acquisition Time	The time the acquisition of data that resulted in this image started
(0018,0050)	Slice Thickness	Nominal slice thickness, in mm
(0020,0032)	Image Position Patient	The x, y, and z coordinates of the upper left hand corner (centre of the first voxel transmitted) of the frame, in mm
(0020,1041)	Slice Location	Relative position of exposure expressed in mm
(0020,0037)	Image Orientation Patient	The direction cosines of the first row and the first column with respect to the patient
(0028,0030)	Pixel Spacing	Physical distance in the patient between the centre of each pixel, specified by a numeric pair in mm